Available online at www.sciencedirect.com
SCIENCE DIRECT®
ELSEVIER
International Journal of Solids and Structures 41 (2004) 6081–6110
INTERNATIONAL JOURNAL OF SOLIDS and STRUCTURES
www.elsevier.com/locate/ijsolstr

A hypoelasto-plastic finite strain simulation of powder compaction processes with density-dependent endochronic model

A.R. Khoei *, A. Bakhshiani

Department of Civil Engineering, Sharif University of Technology, P.O. Box 11365-9313 Tehran, Iran

Received 3 May 2004
Available online 17 June 2004

Abstract

In this paper, a new approach is developed based on an endochronic density-dependent plasticity model for describing the isothermal deformation behavior of metal powder at low homologous temperature. As large deformations are observed in powder compaction processes, the endochronic constitutive model is presented based on large strain plasticity and an integration scheme is established for the rate constitutive equations. Endochronic constitutive equations are established based on coupling between deviatoric and hydrostatic behavior. The elastic response is stated in term of hypoelastic model and endochronic constitutive equations are stated in unrotated frame of reference. Finally, the algorithmic modulus consistent with numerical integration algorithm of constitutive equations is extracted. Although the concept of yield surface has not been explicitly assumed in endochronic theory, it is demonstrated that the cone-cap yield surface can be derived as a special case of the proposed endochronic model. The material parameters in endochronic model are calibrated for two samples of metal powder by fitting the model to reproduce data from true-triaxial compression experiments. The numerical schemes are examined for efficiency and accuracy in the modeling of three powder compaction components.

Keywords: Powder forming; Endochronic plasticity; Hypoelastic model; Large strain; Plastic deformation

1. Introduction

The knowledge of the behavior of powder material undergoing cold compaction is necessary for predicting the final shape and the density distribution within the parts, and for preventing the failures that can occur during the subsequent sintering. Such components vary from simple bush families, which are appropriate for bearing applications, through to complex multi-level parts, which are used in automatic transmission systems. The powder compaction process transforms the loose powder into a compacted

* Corresponding author. Tel.: +98-21-600-5818; fax: +98-21-601-4828.
E-mail address: arkhoei@sharif.edu (A.R. Khoei).

0020-7683/$ - see front matter © 2004 Elsevier Ltd. All rights reserved.
doi:10.1016/j.ijsolstr.2004.05.013

sample with a density increase. Design of a compaction process consists, essentially, in determining the sequence and relative displacements of die and punches in order to achieve this goal. The design process, which has to be done for any new type of piece to be manufactured, could be effectively improved by using a simulation tool, able to predict the mechanical response of the compact along the process.

One of the main ingredients of successful quantitative solution possibilities is an appropriate constitutive modeling of powder, which can reproduce powder material behavior under complicated loading conditions and an accurate and stable integration algorithm for constitutive relation. Several constitutive models for the cold compaction of metal powders have been proposed, including: microscopic models (Fleck et al., 1992, 1995; Ransing et al., 2000; McMeeking et al., 2001), flow formulations (Lewis et al., 1993) and solid mechanics models (Brown and Weber, 1988; Chenot et al., 1990; Brekelmans et al., 1991; Haggblad and Oldenburg, 1994; Lewis and Khoei, 1998). The cap plasticity model used in the modeling of geological and frictional materials, is employed to capture the major features of the response of initially loose metal powders to complex deformation histories which are encountered in the manufacture of engineering components by powder metallurgy techniques. The cone-cap model based on a density-dependent Drucker–Prager yield surface and a non-centered ellipse is developed by Aydin et al. (1996), Khoei and Lewis (1998, 1999), Brandt and Nilsson (1999) and Gu et al. (2001). A double-surface plasticity model is developed by Lewis and Khoei (2001) for the non-linear behavior of powder materials in the concept of the generalized plasticity formulation for the description of cyclic loading. This model is based on the combination of a convex yield surface consisting of a failure envelope, such as a Mohr–Coulomb yield surface and a hardening elliptical yield cap. The model comprises two surfaces, one to reflect shear failure and the other to capture densification.

In the analysis of powder forming problems, the non-linear behavior of powder is adequately described by the cap plasticity model. However, it suffers from a serious deficiency when the stress-point reaches a yield surface. In the flow theory of plasticity, the transition from an elastic state to an elasto-plastic state appears more or less abruptly. For powder material it is very difficult to define the location of yield surface, because there is no distinct transition from elastic to elastic–plastic behavior (Perez-Foguet et al., 2001). Results of experimental test on some hard metal powder show that the plastic effects begin immediately upon loading. Thus, an advanced constitutive theory is necessary to demonstrate this phenomenon. In the present study, an endochronic density-dependent plasticity model is developed to describe the isothermal deformation behavior of metal powder at low homologous temperature.

The endochronic theory deals with the plastic response of materials by means of memory integrals, expressed in terms of memory kernels. Formulation of this theory is based on thermodynamical concepts and provides a unified point of view to describe the elastic–plastic behavior of material, since it places no requirement for a yield surface and 'loading function' to distinguish between loading and unloading. A key ingredient of the theory is that the deformation history is defined with respect to a deformation memory scale called intrinsic time. In the original version of the endochronic theory, proposed by Valanis (1971), the intrinsic time was defined as the path length in the total strain space. The so-called endochronic theory violates the second law of thermodynamics and leads to constitutive relations, which characterize inherently unstable materials (Sandler, 1978; Rivlin, 1981). Aiming at the correction of this deficiency, a new version of the endochronic theory was developed by Valanis (1980) in which the intrinsic time was defined as the path length in the plastic strain space. The new endochronic plasticity was capable of predicting a stress-response to deformation processes, including reversal points in loading in agreement with the experimentally observed mechanical behavior of metals. Also, Valanis demonstrated that an introduction of Dirac delta function into the kernel function leads to a derived result of a yield surface and classical plasticity models of isotropic and kinematic hardening could be derived as a special case of the endochronic theory.

The first implementation of an endochronic theory into a multi-dimensional finite element code was made by Lin et al. (1981), who focused on the original endochronic theory with one term exponential for the kernel function. An implicit finite element algorithm for the modern version of endochronic theory

without a yield surface was developed by Valanis and Fan (1984), which was incrementally non-linear. Also, Watanbe and Atluri (1985) presented an implicit finite element algorithm for the modern endochronic theory. They used the endochronic plasticity with yield surface and the resulting constitutive equations were incrementally linear. An unconditional stable integration scheme of endochronic constitutive equations was proposed by Hsu et al. (1991, 1992) and its ability is examined in the modeling of random non-proportional tests on OFHC copper. Hsu and Griffin (1996) implemented radial return algorithm in integration of endochronic constitutive equations and applied their formulation to finite element micromechanics modeling of a unidirectional metal matrix composite subjected to non-proportional cyclic loading.

The endochronic theory was extended to finite deformation with the concept of the corotational rate and plastic spin by Im and Atluri (1987). They derived the governing equations by using the isoclinic configuration as the intermediate configuration and the corresponding second Piola–Kirchhoff stress tensor. Cases of finite uniaxial compression and torsion were discussed in their work. Wu et al. (1995) incorporated the concepts of corotational rate, corotational integral and plastic spin to endochronic theory and applied it to description of rigid-plastic deformation in thin-walled tubes subjected to finite torsion. Pan et al. (1996) extended the ordinary differential constitutive equations of endochronic theory to simulate elasto-plastic deformation in the range of finite strain using the concept of corotational rate. Different objective rates were incorporated into the theory and cases involving metal tubes under torsion and metal rectangular block under biaxial compression were discussed. An endochronic plasticity theory was developed by Khoei et al. (2003a) to describe the large deformation in finite strain using the concepts of corotational stress rate and the additive decomposition of deformation rate. They derived the constitutive equations for thin-walled tube under torsion to simulate the axial effects for various materials subjected to simple and pure torsional loading. An elasto-plastic and elasto-viscoplastic endochronic theory was extended to large strain range on the basis of the additive decomposition of the strain rate tensor and hypoelasticity by Khoei et al. (2003b). Recently, Khoei et al. (2003c) developed a density-dependent endochronic theory in finite strain plasticity to simulate the compaction process of powder material.

In this paper, the endochronic plasticity theory developed by Khoei et al. (2003c) for powder compaction simulation is extended based on coupling between plastic deviatoric and plastic hydrostatic deformation. The new endochronic model is proposed for a better understanding of the isothermal deformation behavior of metal powder at low homologous temperature. It is demonstrated how the cone-cap plasticity can be generated from the proposed endochronic model by using a special form for the kernel functions. As large deformation is observed in powder compaction process, a hypoelastic–plastic formulation is developed in the context of finite deformation plasticity. Constitutive equations are stated in unrotated frame of reference that greatly simplifies endochronic constitutive relation in finite plasticity. While the explicit treatment of both the integration of constitutive equations and the solution of the equilibrium equation is a common approach in the highly non-linear behavior of powder compaction simulation, an implicit scheme is employed to present the efficiently and accurately the method for this type of non-linear problems. An integration scheme, which is accurate, stable and amenable to consistent linearization is developed. Although the major challenge in the integration of rate constitutive equations in large deformation analysis is to achieve incremental objectivity, it has been trivially achieved. Algorithmic modulus consistent with numerical integration of constitutive equations for the density-dependent endochronic theory is extracted. The implementation of consistent modulus in global tangent stiffness matrix is essential in preserving the quadratic rate of convergence of Newton procedure in solving the equilibrium equations. The material parameters in the constitutive model are calibrated for two samples of metal powder by fitting the model to reproduce data from true-triaxial compression experiments. In order to demonstrate the efficiency and accuracy of the proposed constitutive model and computational algorithms, three powder forming processes are simulated.

The plan of the paper is as follows: in Section 2, the density-dependent endochronic plasticity model is developed to represent the response of metal powder. In Section 3, the implementation of endochronic

plasticity model in large deformation is introduced. In Section 4, the numerical integration of constitutive equations are extracted. Section 5 is devoted to the assessment of the model and computational procedure. In Section 6, some concluding remarks are presented. Finally, the consistent tangent modulus, which has an important role in the convergence rate of global non-linear system of equations is presented in Appendix A.

2. Endochronic constitutive model

Constitutive equations of the endochronic theory for rate-independent, plastically compressible, initially isotropic material due to plastic volumetric and plastic deviatoric deformation can be expressed as

$$\boldsymbol{\sigma}_{\mathrm{dev}} = 2\int_0^{z_{\mathrm{d}}} \Phi_{\mathrm{d}}(z_{\mathrm{d}} - z')\frac{\mathrm{d}\boldsymbol{\varepsilon}^{\mathrm{p}}_{\mathrm{dev}}}{\mathrm{d}z'}\mathrm{d}z' \tag{1}$$

$$\sigma_{\mathrm{h}} = 2\int_0^{z_{\mathrm{h}}} \Phi_{\mathrm{h}}(z_{\mathrm{h}} - z')\frac{\mathrm{d}\varepsilon^{\mathrm{p}}_{\mathrm{vol}}}{\mathrm{d}z'}\mathrm{d}z' - 2\int_0^{z_{\mathrm{h}}} \Psi(z_{\mathrm{h}} - z')\boldsymbol{\sigma}_{\mathrm{dev}} : \frac{\mathrm{d}\boldsymbol{\varepsilon}^{\mathrm{p}}_{\mathrm{dev}}}{\mathrm{d}z'}\mathrm{d}z' \tag{2}$$

where $\Phi_{\mathrm{d}}(z_{\mathrm{d}})$, $\Phi_{\mathrm{h}}(z_{\mathrm{h}})$ and $\Psi(z_{\mathrm{h}})$ are material functions called deviatoric, hydrostatic and coupling hereditary functions. A time scale ς is introduced which is independent of elapsed time, but intrinsically dependent on the deformation of material. It is through this parameter that history effects are introduced into constitutive equations of endochronic theory.

$$\mathrm{d}\varsigma^2 = \mathrm{d}\boldsymbol{\varepsilon}^{\mathrm{p}}_{\mathrm{dev}} : \mathrm{d}\boldsymbol{\varepsilon}^{\mathrm{p}}_{\mathrm{dev}} + \kappa^2 \mathrm{d}\varepsilon^{\mathrm{p}^2}_{\mathrm{vol}} \tag{3}$$

$$\mathrm{d}z_{\mathrm{d}} = \frac{\mathrm{d}\varsigma}{f_{\mathrm{d}}(\eta, p, \theta)} \tag{4}$$

$$\mathrm{d}z_{\mathrm{h}} = \frac{\mathrm{d}\varsigma}{\kappa f_{\mathrm{h}}(\eta, p)} \tag{5}$$

where $f_{\mathrm{d}}(\eta, p, \theta)$ and $f_{\mathrm{h}}(\eta, p)$ are material functions called deviatoric and hydrostatic scale functions. These functions depend on hydrostatic pressure p, with its positive value in tension, Lode's angle θ and relative density η, defined as

$$\theta = \frac{1}{3}\arccos\left(\frac{3\sqrt{3}J_3}{2J_2^{3/2}}\right) \tag{6}$$

$$\eta = \frac{\rho_t}{\rho_{\mathrm{s}}} \tag{7}$$

where J_2 and J_3 are second and third invariants of deviatoric stress tensor, ρ_t is the apparent density in time t and ρ_{s} denotes the solid density of material. The relative density η evolves in time by the following relation

$$\eta = \frac{\eta_0}{J} \tag{8}$$

where η_0 is the initial relative density and J is the third invariant of deformation gradient tensor. In Eq. (3), κ is the coupling parameter between the deviatoric and hydrostatic deformations. In above equations, the total stress tensor is denoted by $\boldsymbol{\sigma}$ and its deviatoric and hydrostatic parts by $\boldsymbol{\sigma}_{\mathrm{dev}}$ and σ_{h}. The symbol $\boldsymbol{\varepsilon}$ represents the total strain tensor by deviatoric and volumetric parts, $\boldsymbol{\varepsilon}_{\mathrm{dev}}$ and $\varepsilon_{\mathrm{vol}}$, respectively. The superscripts 'e' and 'p' indicate the elastic and plastic components, respectively.

The kernel functions $\Phi_{\mathrm{d}}(z_{\mathrm{d}})$, $\Phi_{\mathrm{h}}(z_{\mathrm{h}})$ and $\Psi(z_{\mathrm{h}})$ can be expressed in terms of a Dirichlet series as (Valanis and Peters, 1991)

$$\Phi_{\mathrm{d}}(z_{\mathrm{d}}) = \sum_{i=1}^{\infty} A_i \mathrm{e}^{-\alpha_i z_{\mathrm{d}}} \tag{9}$$

$$\Phi_{\mathrm{h}}(z_{\mathrm{h}}) = \sum_{i=1}^{\infty} B_i \mathrm{e}^{-\beta_i z_{\mathrm{h}}} \tag{10}$$

$$\Psi(z_{\mathrm{h}}) = \sum_{i=1}^{\infty} \frac{C_i}{\kappa f_{\mathrm{h}}} \mathrm{e}^{-\beta_i z_{\mathrm{h}}} \tag{11}$$

with the requirements that A_i, B_i, α_i, β_i and C_i are non-negative for all values of i, and the conditions,

$$\sum_{i=1}^{\infty} \frac{A_i}{\alpha_i} < \infty \tag{12}$$

$$\sum_{i=1}^{\infty} \frac{B_i}{\beta_i} < \infty \tag{13}$$

$$\sum_{i=1}^{\infty} \frac{C_i}{\beta_i} < \infty \tag{14}$$

These conditions ensure the integrability of $\Phi_{\mathrm{d}}(z_{\mathrm{d}})$, $\Phi_{\mathrm{h}}(z_{\mathrm{h}})$ and $\Psi(z_{\mathrm{h}})$ over a finite domain of time scale z. In numerical application m-term Dirichlet series can be used as (Hsu et al., 1991)

$$\Phi_{\mathrm{d}}(z_{\mathrm{d}}) = \sum_{i=1}^{m} A_i \mathrm{e}^{-\alpha_i z_{\mathrm{d}}} \tag{15}$$

$$\Phi_{\mathrm{h}}(z_{\mathrm{h}}) = \sum_{i=1}^{m} B_i \mathrm{e}^{-\beta_i z_{\mathrm{h}}} \tag{16}$$

$$\Psi(z_{\mathrm{h}}) = \frac{1}{\kappa f_{\mathrm{h}}} \sum_{i=1}^{m} C_i \mathrm{e}^{-\beta_i z_{\mathrm{h}}} \tag{17}$$

In above relations, coupling between deviatoric and hydrostatic behavior is introduced in endochronic theory through intrinsic time ς leading to dilatant deformation, which is defined by Eq. (3) and the rate equation (2) through hereditary function $\Psi(z_{\mathrm{h}})$. The role of scale functions $f_{\mathrm{d}}(\eta, p, \theta)$ and $f_{\mathrm{h}}(\eta, p)$ is crucial in the behavior of model. By scaling intrinsic time, these functions cause hardening or softening plastic behavior as a function of hydrostatic pressure, relative density of material and Lode's angle.

2.1. Yield function

The concept of yield surface has not been assumed in the endochronic theory of plasticity but it can be derived implicitly by assuming special forms for the kernel functions of Eqs. (15)–(17). Although the derived yield surface is not used in the integration of the constitutive equations, it is employed in this section to describe the properties of the proposed endochronic plasticity and the effects of $f_{\mathrm{d}}(\eta, p, \theta)$ and $f_{\mathrm{h}}(\eta, p)$ on its behavior.

Consider that the kernel functions $\Phi_{\rm d}(z_{\rm d})$, $\Phi_{\rm h}(z_{\rm h})$ and $\Psi(z_{\rm h})$ are expressed by one term of delta function, they can be written as

$$\Phi_{\rm d}(z_{\rm d}) = \phi_{\rm d}\alpha_1 {\rm e}^{-\alpha_1 z_{\rm d}} = \phi_{\rm d}\delta(z_{\rm d}), \quad \alpha_1 \to \infty \tag{18}$$

$$\Phi_{\rm h}(z_{\rm h}) = \phi_{\rm h}\beta_1 {\rm e}^{-\beta_1 z_{\rm h}} = \phi_{\rm h}\delta(z_{\rm h}), \quad \beta_1 \to \infty \tag{19}$$

$$\Psi(z_{\rm h}) = \frac{1}{\kappa f_{\rm h}}\psi_{\rm h}\beta_1 {\rm e}^{-\beta_1 z_{\rm h}} = \frac{1}{\kappa f_{\rm h}}\psi_{\rm h}\delta(z_{\rm h}), \quad \beta_1 \to \infty \tag{20}$$

where $\delta(x)$ is Dirac delta function and $\phi_{\rm d}$, $\phi_{\rm h}$ and $\psi_{\rm h}$ are positive parameters. Substituting the above relations in Eqs. (1) and (2) and using relations (3)–(5), with some straightforward manipulations leads to the following relation

$$q^2 + \frac{3}{2}\left(\frac{\phi_{\rm d}}{\phi_{\rm h}}\frac{f_{\rm d}}{f_{\rm h}}\right)^2\left(p + \frac{2}{3}\frac{\psi_{\rm h}}{\phi_{\rm d} f_{\rm d}}q^2\right)^2 = \frac{3}{2}\phi_{\rm d}^2 f_{\rm d}^2 \tag{21}$$

where p is the hydrostatic pressure, with positive value in tension, and q is defined as $q = \sqrt{\frac{3}{2}\boldsymbol{\sigma}_{\rm dev} : \boldsymbol{\sigma}_{\rm dev}}$. Although the yield surface has not been explicitly assumed in endochronic theory, introducing delta function to kernels, results implicitly in this concept. In order to present different aspects of Eq. (21), the following specific forms are proposed for the dependence of deviatoric scale function $f_{\rm d}(\eta, p, \theta)$ and hydrostatic scale function $f_{\rm h}(\eta, p)$ on η, p and θ

$$f_{\rm d}(\eta, p, \theta) = h(\theta)\left(c(\eta) - \frac{p}{p_0}\right) \tag{22}$$

$$f_{\rm h}(\eta, p) = (1-\psi)g(\eta) - \psi\frac{p}{\phi_{\rm h}} \tag{23}$$

where p_0 is a positive parameter and ψ is a positive number in the range of 0–1. In Eq. (22), $c(\eta)$ is an increasing function of relative density, defined as

$$c(\eta) = A_c + B_c\eta^{m_c}\frac{\eta - \eta_m}{1 - \eta_m} \tag{24}$$

in which the dependence of $c(\eta)$ on η is a power-law form. In above equation, A_c, B_c, η_m and m_c are material parameters with positive values. In Eq. (22), $h(\theta)$ is defined based on Willam–Warnke function as

$$h(\theta) = \left(\frac{2(e^2-1)\cos\theta + (2e-1)\sqrt{5e^2 - 4e + 4(1-e^2)\cos^2\theta}}{(2e-1)^2 + 4(1-e^2)\cos^2\theta}\right)^{\frac{1}{2}} \tag{25}$$

where e is a parameter of the model. In Eq. (23), $g(\eta)$ is an increasing function of relative density with the following specific form

$$g(\eta) = A_\eta\eta^{m_\eta}\frac{\eta - \eta_m}{1 - \eta_m} \tag{26}$$

where A_η and η_m are positive material parameters. Typical evolution of $f_{\rm d}(\eta, p, \theta)$ and $f_{\rm h}(\eta, p)$ with η and p are plotted in Fig. 1. Introducing Eqs. (22) and (23) into (21) results in a yield function, whose cross sectional shape on meridian plan is plotted in Fig. 2. This yield surface is very similar to the cone-cap yield surface, i.e. a combination of Mohr–Coulomb or Drucker–Prager and elliptical yield surfaces, which has been extensively used by authors to describe the behavior of powder and granular materials (Aydin et al., 1996; Brandt and Nilsson, 1999; Gu et al., 2001; Lewis and Khoei, 2001).

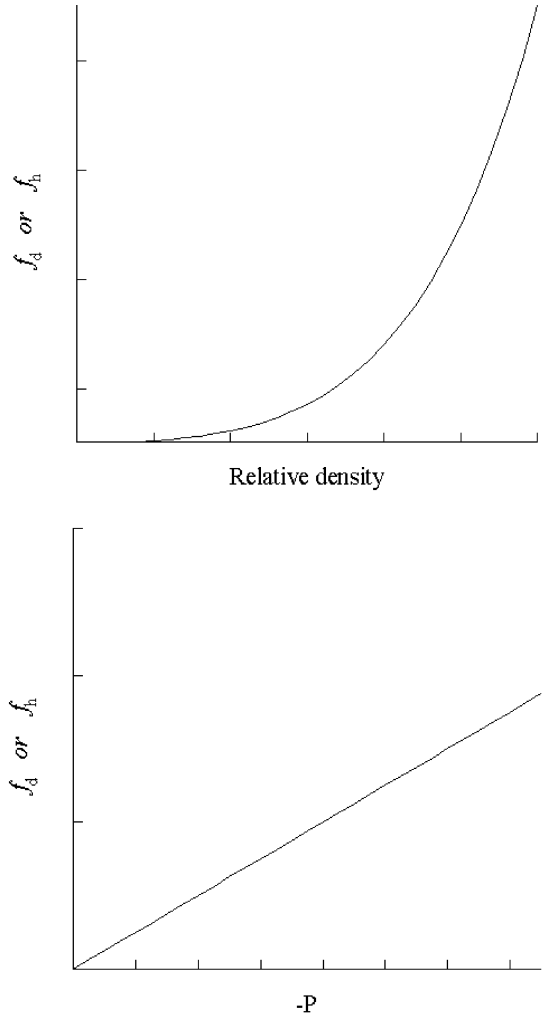

Fig. 1. Typical evolution of f_d and f_h with relative density and hydrostatic pressure.

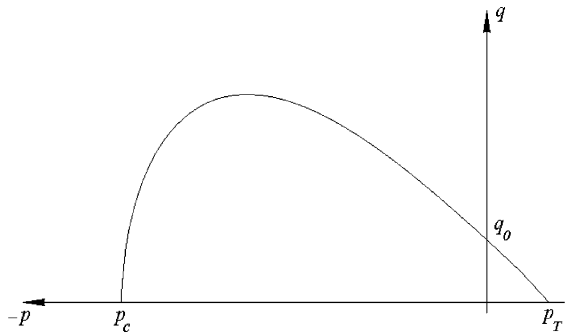

Fig. 2. Trace of a typical yield function on meridian plane.

2.2. Dilatancy condition

The parameters κ and ψ_h in Eqs. (3) and (20) control the coupling between deviatoric and hydrostatic responses in behavior of the model. In this section, the effects of these parameters are discussed and a procedure for their estimation from experimental data are described. Substituting Eqs. (19) and (20) in Eq. (2) yields

$$\sigma_h = \phi_h \kappa f_h \frac{d\varepsilon^p_{vol}}{d\varsigma} - \psi_h \boldsymbol{\sigma}_{dev} : \frac{d\boldsymbol{\varepsilon}^p_{dev}}{d\varsigma} \tag{27}$$

Eliminating $d\varsigma$ between Eqs. (3) and (27) and considering $\boldsymbol{\sigma}_{dev} : d\boldsymbol{\varepsilon}^p_{dev}$ as $\|\boldsymbol{\sigma}_{dev}\| \|d\boldsymbol{\varepsilon}^p_{dev}\| \cos\tau$, we obtain the following relation (Valanis and Peters, 1991)

$$\kappa \frac{d\varepsilon^p_{vol}}{\|d\boldsymbol{\varepsilon}^p_{dev}\|} = \frac{1 - \left(\psi_h \frac{\|\boldsymbol{\sigma}_{dev}\| \cos\tau}{\sigma_h}\right)^2}{\frac{f_h \psi_h |\boldsymbol{\sigma}_{dev}\| \cos\tau}{\sigma_h^2} + \sqrt{\left(\frac{f_h}{\sigma_h}\right)^2 + \left(\frac{\psi_h \|\boldsymbol{\sigma}_{dev}\| \cos\tau}{\sigma_h}\right)^2 - 1}} \tag{28}$$

In particular case of triaxial compression test, when the loading condition occurs, $\cos\tau = 1$ and the dilatancy condition will be reduced to the following condition

$$\psi_h > -\frac{\sigma_h}{\|\boldsymbol{\sigma}_{dev}\|} \tag{29}$$

The two material parameters ψ_h and κ can be determined from the results of triaxial compression test. The constant ψ_h is the ratio of $-\sigma_h/\|\boldsymbol{\sigma}_{dev}\|$ at the initiation of dilatation, where the effect of $d\varepsilon^p_{vol}$ is vanished. After indicating ψ_h, the coupling parameter κ can be computed by substituting the measured dilatancy rate $d\varepsilon^p_{vol}/d\boldsymbol{\varepsilon}^p_{dev}$ into Eq. (28).

2.3. Plastic flow rule

In order to investigate the direction of plastic strain increment in stress space, substitute Eqs. (4), (5), (18), (19) and (20) into Eqs. (1) and (2). It leads to the following relation for increment of plastic strains

$$d\boldsymbol{\varepsilon}^p_{dev} = \frac{d\varsigma}{f_d \phi_d} \boldsymbol{\sigma}_{dev} \tag{30}$$

$$d\varepsilon^p_{vol} = \frac{d\varsigma}{\kappa f_h \phi_h} \left(\sigma_h + \kappa \psi_h \frac{f_h}{\phi_d f_d} \|\boldsymbol{\sigma}_{dev}\|^2\right) \tag{31}$$

The above relations are the flow rule, which is implicitly derived from the proposed endochronic model. The variable $d\varsigma$ can be interpreted as the counterpart of consistency parameter of classical plasticity models. The above relations can be written in (p, q) stress space using the components of flow vector on the meridian plan $\boldsymbol{m} = (m_p, m_q)$ as

$$m_p = \frac{d\varsigma}{\kappa f_h \phi_h} \left(p + \frac{2}{3} \frac{\kappa f_h \psi_h}{\phi_d f_d} q^2\right) \tag{32}$$

$$m_q = \frac{2}{3} \frac{d\varsigma}{f_d \phi_d} q \tag{33}$$

The direction of the plastic flow vector with components (m_p, m_q) does not, in general, coincide with the gradients of yield function (21) and thus, the derived flow rule is non-associative. Applying the higher values for ψ_h, increases the dilatancy in cone region of the yield surface (21).

2.4. Parameter calibration

In this section, the calibration procedure for the endochronic plasticity model is developed based on a series of isostatic, triaxial, direct shear and uniaxial compression tests. In order to relate the material parameters of the proposed endochronic theory to cone-cap plasticity model, substitute Eqs. (22) and (23) in (21) and solve it for p at $q = 0$. It yields to two roots for p, the points of intersection of yield surface with p-axis. The positive root is p_T and negative root is p_c (Fig. 2)

$$p_c = -\phi_{\mathrm{h}} g(\eta) \tag{34}$$

$$p_T = p_0 c(\eta) \tag{35}$$

In Eq. (34), the absolute value of p_c increases as a function of $g(\eta)$. Thus, the evolution of material relative density causes hardening behavior of material. In Eq. (35), the position of p_T is a function of relative density and depends on the parameters of deviatoric scale function. By choosing the non-zero values for parameters of $c(\eta)$, a density-dependent cohesion can be introduced to the endochronic model. Typical evolution of yield surface (21) is shown in Fig. 3 for different values of p_T and p_c in meridian plan. In Eq. (34), a hydrostatic compression test is required to determine the parameters of function $g(\eta)$. The stress–strain curve obtained from this test gives the evolution of hydrostatic compression yield stress p_c as a function of material density.

As the material parameter ψ_{h} is generally a small value relative to ϕ_{d}, the intersection of yield surface with q-axis, defined by q_0 in Fig. 2, can be obtained with good approximation from Eqs. (21)–(23) as

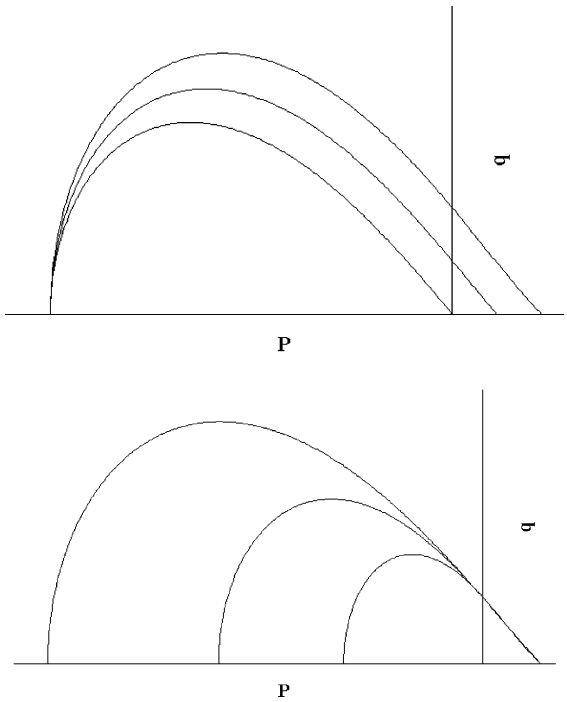

Fig. 3. Trace of cone-cap yield function on the meridian plane for different values of p_T and p_c.

$$q_0 \cong \sqrt{\frac{3}{2}} h(\theta)\phi_d c(\eta) \tag{36}$$

The ratio of q_0/p_T is the slope of cone part of yield surface in meridian plan, shown in Fig. 2, which can be related to the friction angle of material. Considering ϕ_d as a constant known value, p_0 can be determined from Eqs. (35), (36) and friction angle of material, estimated by a standard test, such as hollow cylinder test, simple shear test, or direct shear test. It should be mentioned that ϕ_d and ϕ_h appear as coefficients of f_d and f_h in the yield function, so they are not independent material parameters and can be given any constant values. In Fig. 4, the effect of variation of p_0 on the shape of yield function is shown in meridian plan. It must be noted that q_0, defined in Eq. (36), can be easily related to the cohesion of material. The parameters of function $c(\eta)$ are determined from the variation of material cohesion with relative density, estimated experimentally by simple compression experiments on samples with different initial relative density.

The function $h(\theta)$ controls the shape of yield surface (21) in the deviatoric plane. If $e = 1$, it results in a circular trace of yield function on deviatoric plan. If $e < 1$, it causes triangularity of deviatoric trace along the hydrostatic axis. Fig. 5 shows the trace of yield function on deviatoric plan for different values of shape parameter e. In Fig. 6, the shapes of yield surface are depicted in principal stress space.

It should be mentioned that the behavior of the proposed endochronic model is investigated with one term kernel function. In fact, the application of more than one term in kernel functions adds kinematic hardening to the endochronic model and improves the behavior of model in cyclic loading condition. Obviously, for calibration of material parameters in this case, additional results of cyclic loading test are necessary. Although one term kernel function is sufficient here for the proposed application, the numerical integration of constitutive relations is implemented for the general n-term kernel functions. In addition, it is worth mentioning that as the cone-cap yield surface consists of two different yield functions, special treatment should be made to avoid numerical difficulties in the intersection of these two surfaces, however, the derived yield surface (21) does not have such a drawback.

3. The hypoelasto-plastic finite strain deformation

In order to simulate large deformations in powder compaction processes, the hypoelasto-plastic method is employed based on additive decomposition of rate of deformation into the endochronic plasticity theory. The endochronic model, described in Section 2, is extended to finite strain range using additive elastic–plastic kinematics and a hypoelasto-plastic formulation. The constitutive model is stated in unrotated frame of reference in which achieving incremental objectivity is simple and all the constitutive relations are cast regardless of finite rotations (Johnson and Bammann, 1984; Ponthot, 2002). This approach is rather different with respect to the multiplicative decomposition of the deformation gradient, which is based on the

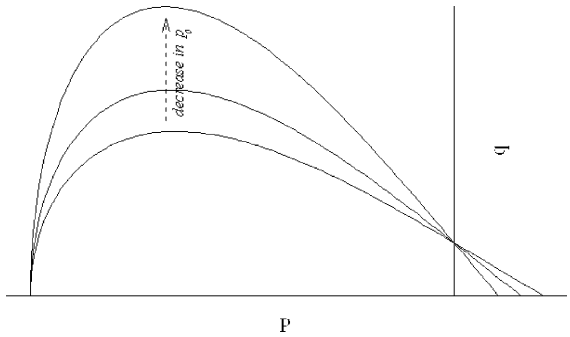

Fig. 4. Trace of cone-cap yield function on the meridian plan for different values of p_0.

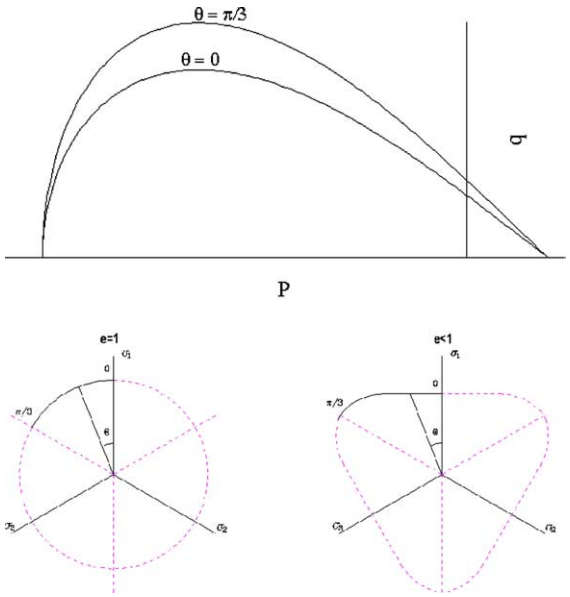

Fig. 5. Trace of cone-cap yield function on deviatoric plan for different values of shape parameter e.

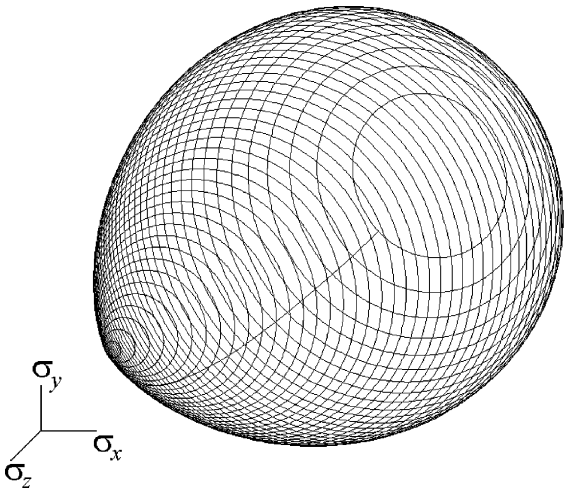

Fig. 6. The shape of cone-cap yield function in principal stress space ($e = 1$).

work of Lee (1969) and used in numerous recent papers (Eve and Reddy, 1994; Fish and Shek, 2000). The proposed integration algorithm treats the elasto-plastic and the elasto-viscoplastic cases in a unified way (Khoei et al., 2003b). This approach greatly simplifies the numerical implementation of endochronic constitutive model.

The hypoelastic material law relates the rate of stress to the rate of deformation. A general form of the hypoelastic relation is defined as

$$\boldsymbol{\sigma}^{\nabla} = f(\boldsymbol{\sigma}, \mathbf{D}) \tag{37}$$

where $\boldsymbol{\sigma}^{\nabla}$ represents any objective rate of Cauchy stress.

There are many objective rates in literature, such as: Jaumann, Truesdell and Green–Naghdi rates. Dienes (1979) has shown that there is spurious oscillation in the stress, which arises directly from the nature of the Jaumann rate. Vanishing of Truesdell rate does not ensure that the invariants of Cauchy stress tensor are constant (Johnson and Bammann, 1984), so in this case further plastic flow will exist. In this formulation the constitutive model is posed in terms of Cauchy stress in unrotated configuration as

$$\hat{\boldsymbol{\sigma}} = \mathbf{R}^{\mathrm{T}}\boldsymbol{\sigma}\mathbf{R} \tag{38}$$

where $\mathbf{R}$ is a proper orthogonal tensor. The conjugate strain rate to $\hat{\boldsymbol{\sigma}}$ is $\widehat{\mathbf{D}}$ defined in unrotated frame of deformation by $\widehat{\mathbf{D}} = \mathbf{R}^{\mathrm{T}}\mathbf{D}\mathbf{R}$. Thus, the hypoelastic part of constitutive equation is

$$\dot{\hat{\boldsymbol{\sigma}}} = \boldsymbol{C}^{\mathrm{e}} : \widehat{\mathbf{D}}^{\mathrm{e}} \tag{39}$$

$$\widehat{\mathbf{D}} = \widehat{\mathbf{D}}^{\mathrm{e}} + \widehat{\mathbf{D}}^{\mathrm{p}} \tag{40}$$

where $\boldsymbol{C}^{\mathrm{e}}$ is the Hook stress–strain tensor defined by

$$\boldsymbol{C}^{\mathrm{e}}_{ijkl} = K\delta_{ij}\delta_{kl} + 2\mu\left(\delta_{ik}\delta_{jl} - \frac{1}{3}\delta_{ij}\delta_{kl}\right) \tag{41}$$

where K and μ are the bulk and shear modulus of material, respectively.

In order to complete the hypoelasto-plastic constitutive equation in the context of finite deformation plasticity, the endochronic constitutive equations are presented in unrotated frame as

$$\hat{\boldsymbol{\sigma}}_{\mathrm{dev}} = 2\int_0^{z_{\mathrm{d}}} \Phi_{\mathrm{d}}(z_{\mathrm{d}} - z')\frac{\widehat{\mathbf{D}}^{\mathrm{p}}_{\mathrm{dev}}}{\dot{z}'}\,\mathrm{d}z' \tag{42}$$

$$\hat{\sigma}_{\mathrm{h}} = 2\int_0^{z_{\mathrm{h}}} \Phi_{\mathrm{h}}(z_{\mathrm{h}} - z')\frac{\widehat{D}^{\mathrm{p}}_{\mathrm{vol}}}{\dot{z}'}\,\mathrm{d}z' - 2\int_0^{z_{\mathrm{h}}} \Psi(z_{\mathrm{h}} - z')\hat{\boldsymbol{\sigma}}_{\mathrm{dev}} : \frac{\widehat{\mathbf{D}}^{\mathrm{p}}_{\mathrm{dev}}}{\dot{z}'}\,\mathrm{d}z' \tag{43}$$

$$\dot{z}_{\mathrm{d}} = \frac{\dot{\varsigma}}{f_{\mathrm{d}}(\eta, p, \theta)} \tag{44}$$

$$\dot{z}_{\mathrm{h}} = \frac{\dot{\varsigma}}{f_{\mathrm{h}}(\eta, p)} \tag{45}$$

$$\dot{\varsigma}^2 = \widehat{\mathbf{D}}^{\mathrm{p}}_{\mathrm{dev}} : \widehat{\mathbf{D}}^{\mathrm{p}}_{\mathrm{dev}} + \kappa^2(\widehat{D}^{\mathrm{p}}_{\mathrm{vol}})^2 \tag{46}$$

where

$$\hat{\boldsymbol{\sigma}} = \hat{\boldsymbol{\sigma}}_{\mathrm{dev}} + \hat{\sigma}_{\mathrm{h}}\mathbf{I} \tag{47}$$

$$\hat{\boldsymbol{\sigma}}_{\mathrm{dev}} = \mathrm{dev}[\hat{\boldsymbol{\sigma}}] \tag{48}$$

$$\hat{\sigma}_{\mathrm{h}} = \frac{1}{3}\mathrm{tr}[\hat{\boldsymbol{\sigma}}] \tag{49}$$

$$\widehat{\mathbf{D}}^{\mathrm{p}} = \widehat{\mathbf{D}}^{\mathrm{p}}_{\mathrm{dev}} + \widehat{D}^{\mathrm{p}}_{\mathrm{vol}} I \tag{50}$$

$$\widehat{\mathbf{D}}^{\mathrm{p}}_{\mathrm{dev}} = \mathrm{dev}[\widehat{\mathbf{D}}^{\mathrm{p}}] \tag{51}$$

$$\widehat{D}^{\mathrm{p}}_{\mathrm{vol}} = \mathrm{tr}[\widehat{\mathbf{D}}^{\mathrm{p}}] \tag{52}$$

and $\mathrm{dev}[\cdot] = [\cdot] - \frac{1}{3}\mathrm{tr}[\cdot]\mathbf{I}$, with $\mathbf{I}$ denoting the spatial metric tensor.

4. Numerical integration of constitutive equations

The major challenge in the integration of the rate constitutive equations in finite strain range is to achieve incremental objectivity. The implementation of objective stress rates in constitutive equations results in objective formulation only in the limit of very small time step (Hughes and Winget, 1980). As the standard time discretization procedures cannot be lead to incremental objectivity, one efficient way to overcome this problem is to state constitutive equations in corotational frame. Assuming that the variables of the model at step n and the incremental displacement field $\Delta u = {}^{n+1}x - {}^{n}x$ at load step $n+1$ are known, the updated value of different variables of the model will be calculated at load step $n+1$. The left superscript refers to the load step which is omitted for current step.

Applying the backward Euler scheme to Eq. (39) yields

$$\hat{\boldsymbol{\sigma}} = {}^{n}\hat{\boldsymbol{\sigma}} + \boldsymbol{C}^{\mathrm{e}} : \widehat{\mathbf{D}}^{\mathrm{e}}\Delta t \tag{53}$$

$$\Delta\hat{\boldsymbol{\sigma}} = \boldsymbol{C}^{\mathrm{e}} : \Delta\hat{\mathbf{d}}^{\mathrm{e}} = \boldsymbol{C}^{\mathrm{e}} : (\Delta\hat{\mathbf{d}} - \Delta\hat{\mathbf{d}}^{\mathrm{p}}) \tag{54}$$

in which the corotational increment of $\mathbf{D}$ is given based on the midpoint rule as

$$\Delta\hat{\mathbf{d}} = \Delta t\widehat{\mathbf{D}} = \frac{1}{2}\left(\Delta\mathbf{U}\,{}^{n+\frac{1}{2}}\mathbf{U}^{-1} + {}^{n+\frac{1}{2}}\mathbf{U}^{-1}\Delta\mathbf{U}\right) \tag{55}$$

where $\Delta\mathbf{U} = {}^{n+1}\mathbf{U} - {}^{n}\mathbf{U}$ and ${}^{n+\frac{1}{2}}\mathbf{U} = \frac{1}{2}({}^{n+1}\mathbf{U} + {}^{n}\mathbf{U})$.

One of the most important parts of numerical scheme is numerical integration of endochronic constitutive equations. Substituting Eqs. (15)–(17) in (42) and (43) give

$$\hat{\boldsymbol{\sigma}}_{\mathrm{dev}} = 2\sum_{r=1}^{m}\int_0^{z_{\mathrm{d}}} A_r \mathrm{e}^{-\alpha_r(z_{\mathrm{d}}-z')}\frac{\widehat{\mathbf{D}}^{\mathrm{p}}_{\mathrm{dev}}}{\dot{z}'}\,\mathrm{d}z' \tag{56}$$

$$\hat{\sigma}_{\mathrm{h}} = 2\sum_{i=1}^{m}\int_0^{z_{\mathrm{h}}} B_i \mathrm{e}^{-\beta_i(z_{\mathrm{h}}-z')}\frac{\widehat{D}^{\mathrm{p}}_{\mathrm{vol}}}{\dot{z}'}\,\mathrm{d}z' - 2\sum_{i=1}^{m}\int_0^{z_{\mathrm{h}}}\frac{1}{\kappa f_{\mathrm{h}}} C_i \mathrm{e}^{-\beta_i(z_{\mathrm{h}}-z')}\hat{\boldsymbol{\sigma}}_{\mathrm{dev}} : \frac{\widehat{\mathbf{D}}^{\mathrm{p}}_{\mathrm{dev}}}{\dot{z}'}\,\mathrm{d}z' \tag{57}$$

In order to integrate Eqs. (56) and (57) numerically, the loading is divided into n steps, thus

$$\hat{\boldsymbol{\sigma}}^{r}_{\mathrm{dev}}({}^{n}z_{\mathrm{d}}) = 2\sum_{k=1}^{n}\frac{A_r}{\alpha_r}\frac{{}^{k}\left(\Delta\hat{\mathbf{d}}^{\mathrm{p}}_{\mathrm{dev}}\right)}{{}^{k}\Delta z_{\mathrm{d}}}\left[\mathrm{e}^{-\alpha_r({}^{n}z_{\mathrm{d}}-{}^{k}z_{\mathrm{d}})} - \mathrm{e}^{-\alpha_r({}^{n}z_{\mathrm{d}}-{}^{k-1}z_{\mathrm{d}})}\right] \tag{58}$$

$$\hat{\boldsymbol{\sigma}}_{\mathrm{dev}}({}^{n}z_{\mathrm{d}}) = \sum_{r=1}^{m}\hat{\boldsymbol{\sigma}}^{r}_{\mathrm{dev}}({}^{n}z_{\mathrm{d}}) \tag{59}$$

$$\begin{aligned}\hat{\sigma}^{i}_{\mathrm{h}}({}^{n}z_{\mathrm{h}}) = {} & 2\sum_{k=1}^{n}\frac{B_i}{\beta_i}\frac{{}^{k}\left(\Delta\hat{d}^{\mathrm{p}}_{\mathrm{vol}}\right)}{{}^{k}\Delta z_{\mathrm{h}}}\left[\mathrm{e}^{-\beta_i({}^{n}z_{\mathrm{h}}-{}^{k}z_{\mathrm{h}})} - \mathrm{e}^{-\beta_i({}^{n}z_{\mathrm{h}}-{}^{k-1}z_{\mathrm{h}})}\right] - 2\sum_{k=1}^{n}\frac{1}{\kappa f^{k}_{\mathrm{h}}}\frac{C_i}{\beta_i} \\ & \times\frac{{}^{k}\hat{\boldsymbol{\sigma}}_{\mathrm{dev}} : {}^{k}\left(\Delta\hat{\mathbf{d}}^{\mathrm{p}}_{\mathrm{dev}}\right)}{{}^{k}\Delta z_{\mathrm{h}}}\left[\mathrm{e}^{-\beta_i({}^{n}z_{\mathrm{h}}-{}^{k}z_{\mathrm{h}})} - \mathrm{e}^{-\beta_i({}^{n}z_{\mathrm{h}}-{}^{k-1}z_{\mathrm{h}})}\right]\end{aligned} \tag{60}$$

$$\hat{\sigma}_{\mathrm{h}}({}^{n}z_{\mathrm{h}}) = \sum_{i=1}^{m} \hat{\sigma}_{\mathrm{h}}^{i}({}^{n}z_{\mathrm{h}}) \tag{61}$$

It is worth mentioning that the striking feature of the above scheme is the direct integration of hereditary function. Such a procedure, in general leads to more accurate results with much smaller number of increments. Eqs. (58) and (59) can be simplified as

$$\hat{\boldsymbol{\sigma}}_{\mathrm{dev}}^{r}({}^{n}z_{\mathrm{d}}) = \hat{\boldsymbol{\sigma}}_{\mathrm{dev}}^{r}({}^{n-1}z_{\mathrm{d}})\mathrm{e}^{-\alpha_r {}^{n}\Delta z_{\mathrm{d}}} + 2\frac{A_r}{\alpha_r}\frac{{}^{n}\left(\Delta\hat{\mathbf{d}}_{\mathrm{dev}}^{\mathrm{p}}\right)}{{}^{n}\Delta z_{\mathrm{d}}}(1-\mathrm{e}^{-\alpha_r {}^{n}\Delta z_{\mathrm{d}}}) \tag{62}$$

$$\hat{\sigma}_{\mathrm{h}}^{i}({}^{n}z_{\mathrm{h}}) = \hat{\sigma}_{\mathrm{h}}^{i}({}^{n-1}z_{\mathrm{h}})\mathrm{e}^{-\beta_i {}^{n}\Delta z_{\mathrm{h}}} + 2\frac{B_i}{\beta_i}\frac{{}^{n}\left(\Delta\hat{d}_{\mathrm{vol}}^{\mathrm{p}}\right)}{{}^{n}\Delta z_{\mathrm{h}}}(1-\mathrm{e}^{-\beta_i {}^{n}\Delta z_{\mathrm{h}}}) - \frac{2}{\kappa^{n} f_{\mathrm{h}} {}^{n}\Delta z_{\mathrm{h}}}\frac{C_i}{\beta_i}\left({}^{n-1}\hat{\boldsymbol{\sigma}}_{\mathrm{dev}} : {}^{n}\left(\Delta\hat{\mathbf{d}}_{\mathrm{dev}}^{\mathrm{p}}\right)\right)(1-\mathrm{e}^{-\beta_i {}^{n}\Delta z_{\mathrm{h}}}) \tag{63}$$

The incremental form of endochronic constitutive equations can be obtained from Eqs. (62) and (63) by taking step $n+1$ as current step. The incremental equations which is necessary in the numerical modeling of initial strain are as follows

$$\Delta\hat{\boldsymbol{\sigma}}_{\mathrm{dev}} = \sum_{r=1}^{m} {}^{n}\left(\hat{\boldsymbol{\sigma}}_{\mathrm{dev}}^{r}\right)(\mathrm{e}^{-\alpha_r \Delta z_{\mathrm{d}}} - 1) + 2\frac{\Delta\hat{\mathbf{d}}_{\mathrm{dev}}^{\mathrm{p}}}{\Delta z_{\mathrm{d}}}\sum_{r=1}^{m}\frac{A_r}{\alpha_r}(1-\mathrm{e}^{-\alpha_r \Delta z_{\mathrm{d}}}) \tag{64}$$

$$\Delta\hat{\sigma}_{\mathrm{h}} = \sum_{i=1}^{m} {}^{n}\left(\hat{\sigma}_{\mathrm{h}}^{i}\right)(\mathrm{e}^{-\beta_i \Delta z_{\mathrm{h}}} - 1) + 2\frac{\Delta\hat{d}_{\mathrm{vol}}^{\mathrm{p}}}{\Delta z_{\mathrm{h}}}\sum_{r=1}^{m}\frac{B_i}{\beta_i}(1-\mathrm{e}^{-\beta_i \Delta z_{\mathrm{h}}}) - \frac{2({}^{n}\hat{\boldsymbol{\sigma}}_{\mathrm{dev}} : \Delta\hat{\mathbf{d}}_{\mathrm{dev}}^{\mathrm{p}})}{\kappa^{n+1} f_{\mathrm{h}} \Delta z_{\mathrm{h}}}\sum_{r=1}^{m}\frac{C_i}{\beta_i}(1-\mathrm{e}^{-\beta_i \Delta z_{\mathrm{h}}}) \tag{65}$$

$$\Delta\hat{\boldsymbol{\sigma}} = \boldsymbol{C}^{\mathrm{e}} : (\Delta\hat{\mathbf{d}} - \Delta\hat{\mathbf{d}}^{\mathrm{p}}) \tag{66}$$

$$\Delta\varsigma^2 = \Delta\hat{\mathbf{d}}_{\mathrm{dev}}^{\mathrm{p}} : \Delta\hat{\mathbf{d}}_{\mathrm{dev}}^{\mathrm{p}} + \kappa^2\left(\Delta\hat{d}_{\mathrm{vol}}^{\mathrm{p}}\right)^2 \tag{67}$$

$$\Delta z_{\mathrm{d}} = \frac{\Delta\varsigma}{f_{\mathrm{d}}({}^{n+1}\eta, {}^{n+1}p, {}^{n+1}\theta)} \tag{68}$$

$$\Delta z_{\mathrm{h}} = \frac{\Delta\varsigma}{f_{\mathrm{h}}({}^{n+1}\eta, {}^{n+1}p)} \tag{69}$$

A set of seven algebraic equations can be solved for the unknowns values of $\Delta\hat{\mathbf{d}}_{\mathrm{dev}}^{\mathrm{p}}$ and $\Delta\hat{d}_{\mathrm{h}}^{\mathrm{p}}$ by applying the Newton–Raphson method. Once $\Delta\hat{\mathbf{d}}^{\mathrm{p}}$ is known, the corotational increment of stress tensor is derived from Eq. (66). The value of stresses will be then calculated from relations $\hat{\boldsymbol{\sigma}} = {}^{n}\hat{\boldsymbol{\sigma}} + \Delta\hat{\boldsymbol{\sigma}}$ and $\boldsymbol{\sigma} = \mathbf{R}\hat{\boldsymbol{\sigma}}\mathbf{R}^{\mathrm{T}}$.

It can be seen from Eq. (55) that the proposed scheme is trivially incrementally objective. In the case of rigid body motion, ${}^{n+1}\mathbf{U} = {}^{n}\mathbf{U}$ and from Eq. (55) $\widehat{\mathbf{D}} = 0$, thus the stress tensor will be exactly updated by relation ${}^{n+1}\boldsymbol{\sigma} = \Delta\mathbf{R}\,{}^{n}\boldsymbol{\sigma}\Delta\mathbf{R}^{\mathrm{T}}$. It should be noted that in this scheme the rotation tensor $\mathbf{R}$ is exactly computed from the polar decomposition and not from the numerical integration of rate equation $\dot{\omega} = \Omega\omega$, with Ω denoting a spin tensor and ω indicating an orthogonal rotation tensor.

5. Model assessment and numerical results

In order to illustrate the efficiency and accuracy of the material model and numerical schemes, the powder compaction simulation of a multi-level, shaped tablet and cylindrical MH-100 iron powder components are analysed numerically. The material parameters in the constitutive model are calibrated for two samples of metal powder by fitting the model to reproduce data from true-triaxial compression experiments. The endochronic constitutive equations and the proposed numerical integration, described in Sections 2–4, along with the consistent linearization schemes, presented in Appendix A, have been implemented in a non-linear finite element code to evaluate the capability of the model in simulating powder compaction process.

5.1. A multi-level component

The first example is the simulation of a multi-level compaction process chosen to demonstrate the performance of the present formulation for the complicated die geometry of a multi-level component. The experimental data are obtained from a set of compaction experiments on an iron-based powder (95% by weight) performed by Doremus et al. (1995). Both isostatic compaction and triaxial tests were driven. The raw material is composed of iron, copper, wax and zinc stearate, these two last components being admixed as internal lubricants. The density of the solid phase was about 7.54 g/cm^3 and the tap density powder was about 3.67 g/cm^3.

Box 1. Endochronic material parameters. The mixed iron powder

Young modulus: $E(\eta) = E_0\left(\frac{\eta-\eta_e}{1-\eta_e}\right)^3$, $E_0 = 18,000$ MPa, $\eta_e = 0.25$
Poisson ratio $= 0.35$
Initial apparent density $= 3.67$ g/cm^3
Solid density $= 7.54$ g/cm^3
Hereditary function parameters:
$A_1 = 300,000$ MPa
$\alpha_1 = 1000$
$B_1 = 116,700$ MPa
$\beta_1 = 300$
Deviatoric scale function parameters: $a_1 = 1.5$, $a_2 = 0$
Hydrostatic scale function parameters: $m = 7.8$, $\eta_m = 0.4$

The particles had an irregular shape and their size was between 10 and 100 μm. The compacted specimen has an initial height of $H_0 = 42$ cm and diameter of $D_0 = 20$ cm. Triaxial tests consisted of an initial isostatic compaction step up to pressure value of 400 MPa followed by a subsequent uniaxial compaction step carried out by keeping pressure constant and increasing the axial stress up to a maximum value of 1250 MPa.

The powder material is modeled by endochronic plasticity with one term for deviatoric and hydrostatic hereditary functions and isotropic elastic properties. The scale functions $f_{\rm d}(\eta)$ and $f_{\rm h}(\eta)$ are determined from the material properties in terms of relative density. These functions have the highly non-linear forms to cause the hardening behavior of the deviatoric and volumetric plastic response. The following forms, which are appropriate for metal powder, are proposed for the deviatoric and hydrostatic scale functions

$$f_{\mathrm{d}}(\eta) = \eta + a_1\eta^2 + a_2\eta^3 \tag{70}$$

$$f_{\mathrm{h}}(\eta) = \eta^m \frac{\eta - \eta_m}{1 - \eta_m} \tag{71}$$

The parameters of hydrostatic scale function (m and η_m) can be calculated by fitting the response of model to the volumetric strain versus hydrostatic pressure curve obtained from the isostatic compression test. Having determined the parameters of $f_{\mathrm{h}}(\eta)$, the response of the model will be fitted to the results of triaxial test, in order to obtain the parameters of $f_{\mathrm{d}}(\eta)$. The material properties for simulation of powder are given in Box 1.

Fig. 7(a) presents the evolution of the density versus hydrostatic pressure. This evolution is the characteristic of metal powders. The experimental and numerical results are compared for the isostatic

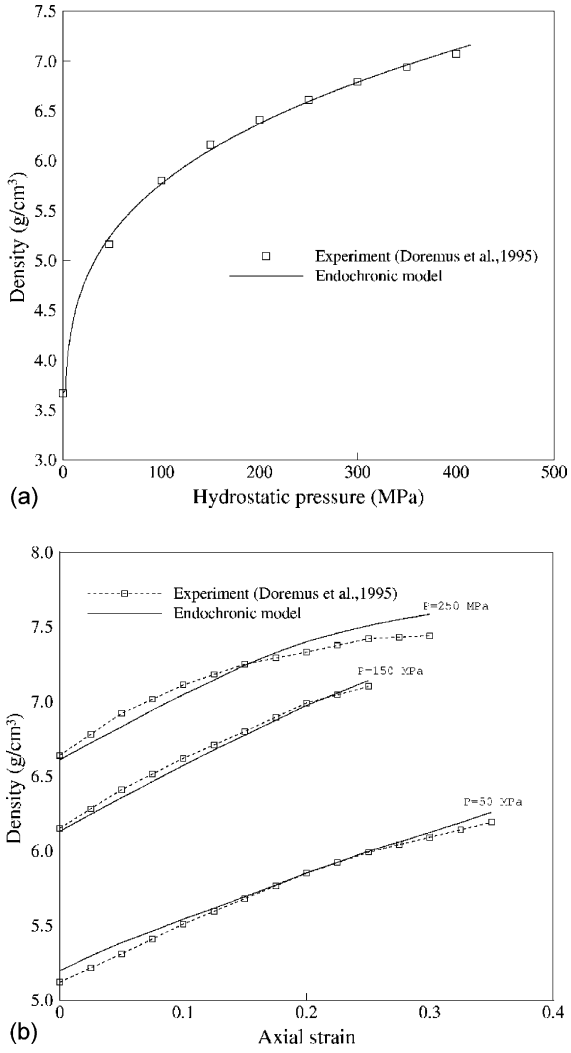

Fig. 7. (a) Density versus hydrostatic pressure during isostatic compaction, (b) density versus axial strain in triaxial tests at given confining pressure.

compression step. The applicability of the proposed endochronic theory to handle the volumetric terms is evident in this figure. Fig. 7(b) corresponds to the complete triaxial compression tests. The density versus axial strain curves are plotted for different values of the hydrostatic pressure attained at the end of isostatic compression step. Remarkable agreements between experimental and numerical results are obtained.

The numerical results are obtained for a multi-level compaction process by Oliver et al. (1996). The simulation is performed with the powder material parameters presented in Box 1. The initial density at the start of simulation is 2.94 g/cm^3. The compact specimen is a bearing used in the automotive industry whose axisymmetric geometry is shown in Fig. 8. The initial and final shapes are plotted in this figure with dashed and full lines. The compaction is performed by means of the action of five punches, labeled a, b, c, d and e in Fig. 8(a). The component is modeled by 2D axisymmetric structured mesh of 813 bilinear elements. Friction effects are considered through a Coulomb's friction model with a friction coefficient of $\mu = 0.1$ (Oliver et al., 1996). A numerical model of the frictional contact based on penalty approach is used to simulate sliding resistance at the tool–workpiece interface. The deformed mesh at the final stage of compaction is plotted in Fig. 8(b). In Fig. 8(c), the relative density contour at the final stage of compaction process is presented. The fairly uniform distribution of relative density is also found by Oliver et al. (1996). A lower relative density distribution is detected at the top part of the sample. The range of the variation of relative density in the sample is similar to those presented by Oliver et al. (1996).

5.2. A shaped tablet component

The second example demonstrates the performance of the present formulation in complicated die geometry and simultaneous high distortional and volumetric deformation of elements in a shaped tablet component. The powder material is modeled using endochronic plasticity with the deviatoric and hydrostatic scale functions defined by Eqs. (70) and (71). The material properties for simulation of powder are given in Box 1. The endochronic material parameters are used to simulate the compaction process of a shaped tablet component, whose axisymmetric geometry is shown in Fig. 9(a). The geometry is used by

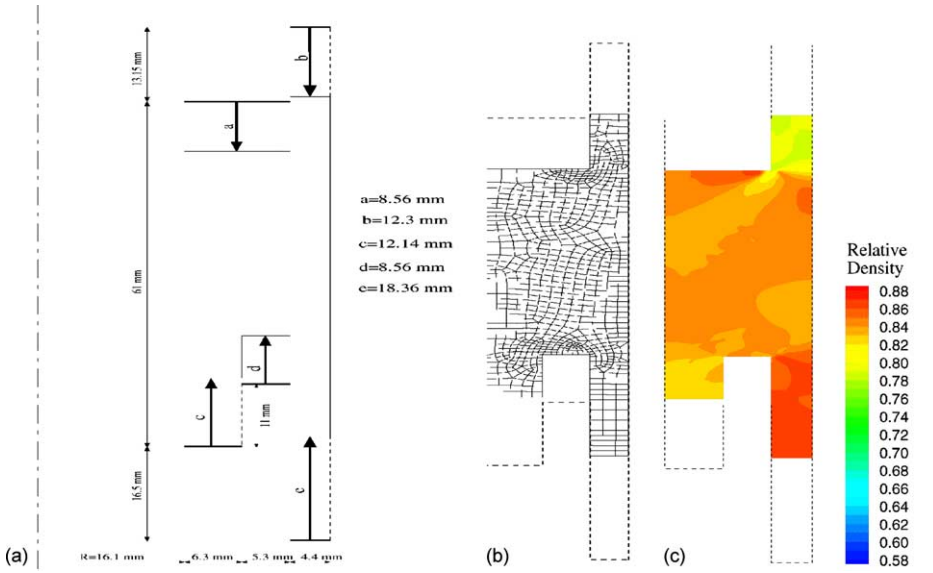

Fig. 8. A multi-level component: (a) geometry and loading description (after Oliver et al., 1996), (b) final deformed mesh, (c) the density distribution at final stage of compaction.

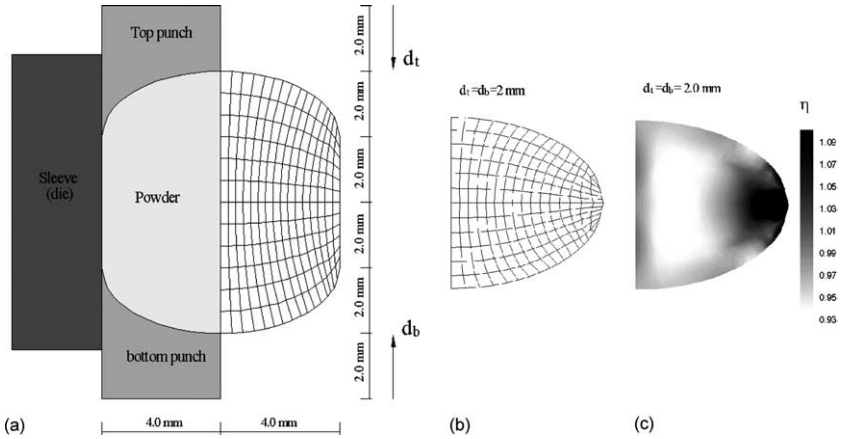

Fig. 9. A shaped tablet component: (a) geometry and loading description (after Lewis and Khoei, 2001), (b) final deformed mesh, (c) the density distribution at final stage of compaction.

Lewis and Khoei (2001) to show the applicability of their formulation in tablet pressing process. The Coulomb friction coefficient is assumed $\mu = 0.08$. The compaction simulation is performed by means of the upper and lower punches. Some problems are caused by discontinuities in geometry, for example the flow around corners and the multi-punch setup.

The deformed mesh at the final stage of compaction is plotted in Fig. 9(b). The relative density contour at the final stage of compaction is presented in Fig. 9(c). From the contour of final stage of compaction, it can be observed that the density in the right hand region of tablet is greater than other parts while regions with low density appear between high-density regions. The distribution of density in final stage of compaction is a bit different from results reported by Lewis and Khoei (2001). These discrepancies can be related to different treatments of friction between powder and punches. While in the present simulation contact between powder and punches is modeled with Coulomb friction of $\mu = 0.08$, in this reference the relative movement between powder and punches is restrained.

5.3. Compaction process of MH-100 iron powder component

The last example describes the applicability of endochronic model in determining the material parameters for dry MH-100 iron powder and predictive capability of the model in simulating the powder compaction process. The material parameters are calibrated by fitting the endochronic model to reproduce the data from the simple compression experiments. Since such experiments on powder materials typically result in non-homogeneous deformations, the fitting procedure requires numerical simulation of the experiments. Gu et al. (2001) produced the material parameters of the MH-100 iron powder for their cone-cap plasticity using the true-triaxial compression experiments, torsion ring-shear experiments, and simple compression experiments.

In order to determine the endochronic material properties in terms of relative density, the following specific forms are proposed for the dependence of deviatoric scale function $f_{\mathrm{d}}(\eta, p)$ and hydrostatic scale function $f_{\mathrm{h}}(\eta, p)$ on η and p

$$f_{\mathrm{d}}(\eta, p) = c(\eta) - \frac{p}{p_0} \tag{72}$$

$$f_{\mathrm{h}}(\eta, p) = (1 - \psi) g(\eta) - \psi \frac{p}{\phi_{\mathrm{h}}} \tag{73}$$

where $c(\eta)$ and $g(\eta)$ are the increasing functions of relative density, defined as

$$c(\eta) = A_c \eta^{m_c} \frac{\eta - \eta_0}{1 - \eta_0}$$
$$g(\eta) = A_g \eta^{m_g} \frac{\eta - \eta_0}{1 - \eta_0} \tag{74}$$

where A_c, A_g, m_c and m_g are material parameters with positive values.

5.3.1. Material parameters of MH-100 iron powder

In order to determine the endochronic material parameters for the consolidation mechanism, the data is obtained from experiments conducted with a high-pressure true-triaxial apparatus developed by Gu et al. (2001). Fig. 10(a) shows a schematic top view of the apparatus. During an experiment, powder is poured into the cubical cavity created by the blocks. Blocks 1 and 2 are angled sliding blocks sitting on the corresponding angled guiding-blocks. When the top block (not shown) moves downward in the 3-direction, sliding blocks 1 and 2 move inward in the 1-direction and 2-direction, respectively, and the powder in the initially cubical cavity is compressed in three orthogonal directions (Gu et al., 2001). The amount of compression in each of the lateral directions can be controlled by changing the angles of the sliding and guiding angled blocks. A plot of proportional strain paths attainable in the apparatus with the available angles blocks is shown in Fig. 10(b). The notation $x°/y°$ denotes the angles of the blocks in the 1- and 2-directions, respectively.

In order to perform the numerical simulations of the true-triaxial tests on MH-100 iron powder, a single three dimensional element is numerically modeled using endochronic plasticity. The simulations are carried out by subjecting an eight-noded brick element to different principal stretchings D_{11}, D_{22}, D_{33} acting on sides normal to the 1-, 2- and 3-directions. The relative values of the applied stretchings corresponding to the different combinations of angled blocks are given in Table 1. The Young's modulus and Poisson's ratio of

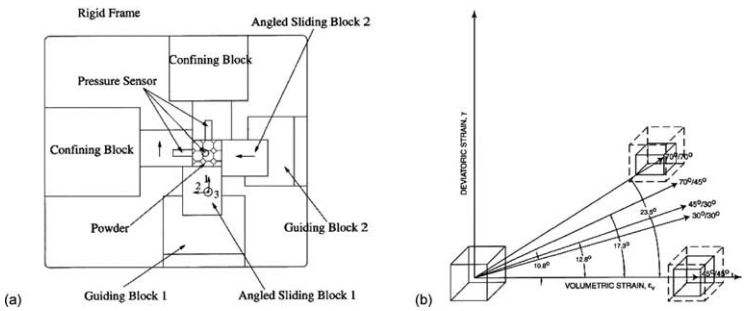

Fig. 10. (a) A schematic of the true-triaxial compression apparatus (Gu et al., 2001), (b) strain paths achievable in the true-triaxial compression experiments.

Table 1
The values of applied stretchings corresponding to different combinations of angled blocks

	D_{11}	D_{22}	D_{33}
45°/45°	−1.0	−1.0	−1.0
30°/30°	−1.732	−1.732	−1.0
70°/70°	−0.364	−0.364	−1.0
70°/30°	−0.364	−1.732	−1.0
70°/45°	−0.364	−1.0	−1.0
30°/45°	−1.732	−1.0	−1.0

MH-100 iron powder compacts have been experimentally determined by Brown and Weber (1988), which are used in the following simulations. The endochronic material parameters are estimated by fitting the response of model to the stress–strain curves obtained from the true-triaxial tests. Gu et al. (2001) measured the normal strains $\{\varepsilon_1, \varepsilon_2, \varepsilon_3\}$ and compressive normal stresses $\{\sigma_1, \sigma_2, \sigma_3\}$ in each experiment for the different angled block arrangements. The hydrostatic scale function parameters corresponding to the cap part of cone-cap plasticity are obtained as

$$g(\eta) = \eta^{2.5}\frac{\eta - 0.45}{1 - 0.45}, \quad \phi_{\mathrm{h}} = 500 \text{ MPa}, \quad \psi = 0.5$$

Fig. 11 shows a comparison between the calculated and measured stress–strain curves for the different deformation rate histories. For example, Fig. 11(a) shows the experimental results with the 45°/45° angled block arrangement. The corresponding stress versus strain curves are almost identical in all three directions. Thus, the 45°/45° angled block arrangement corresponds to an approximate hydrostatic compression test. Fig. 11(d) shows the stress versus strain curves for the experiment with the 70°/30° angled block arrangement. In this case, the stress–strain curves in three directions are all different from each other, and a true-triaxial stress state is achieved. The numerical results for all the different triaxial loading paths are in very good agreement with the experiments.

In order to evaluate the deviatoric scale function parameters corresponding to the cone part of cone-cap plasticity, the data is obtained from experiments conducted with the distortion mechanism of a torsion ring-shear apparatus, as well as by using data obtained from simple compression experiments on unsintered compacts with different initial relative densities (Gu et al., 2001). A schematic of the apparatus is shown in Fig. 12. In this apparatus, a thin hollow cylindrical specimen of the powder of inner and outer diameters of 63.50 and 69.85 mm, respectively, is confined between two floating concentric confining rings, and two annular punches. One of the annular punches is fixed, and the other can be displaced in the axial direction as well as twisted about its axis to subject the powder specimen to various combinations of axial compression and twist. Gu et al. (2001) performed a set of experiments in which the ring specimens were first axially compressed under different normal pressures to different initial relative densities, and the compressed powder rings are then sheared while keeping the corresponding normal pressures constant. Based on the torsional portion of these experiments, the nominal residual friction coefficient of MH-100 powder was estimated 0.45 (Gu et al., 2001). Applying the procedure described in Section 2.4, choosing $\phi_{\mathrm{d}} = 90$ and using Eqs. (34) and (35) results in the value of 245 MPa for p_0.

In order to evaluate the other deviatoric scale function parameters, i.e. $c(\eta)$, the variation of material cohesion with relative density is obtained using simple compression experiments on samples with different initial relative density (Gu et al., 2001). Cylindrical specimen is formed with a diameter of 25.4 mm and height of 15 mm in a uniaxial strain compaction apparatus. Unconfined simple compression experiments are then performed on these specimens. An estimation of the cohesion with relative density for MH-100 iron powder is shown in Fig. 13. The curve plotted in this figure is the fit of our proposed functional form for $c(\eta)$

$$c(\eta) = 1.4\eta^3\frac{\eta - 0.45}{1 - 0.45}$$

In order to illustrate the efficiency and accuracy of the endochronic material model in large strain range, the uniaxial compaction experiment is analysed numerically. The finite element modeling of specimen is performed using 2D axisymmetric structured mesh of 625 bilinear elements, as illustrated in Fig. 14. As a displacement based formulation is used, the implementation of loading is achieved by the use of prescribed nodal displacements. The direction of this displacement is in a vertical plane which represents the axial punch load. Fixed nodal values are employed to represent the fixed bottom punch. Simulation is performed with powder material parameters presented in this section using different initial relative densities of 0.696,

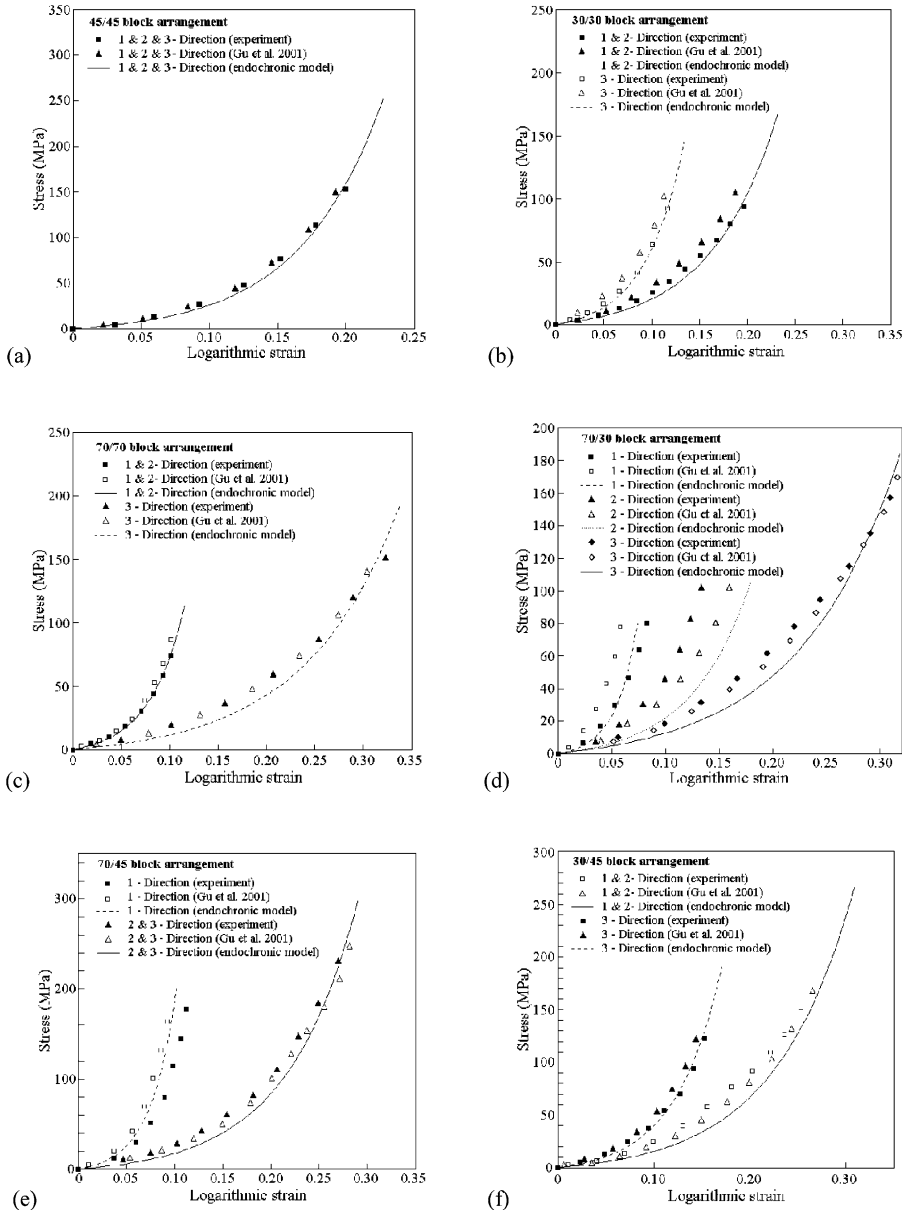

Fig. 11. Comparison of the calculated stress–strain responses against measured and other simulated results in the true-triaxial compression experiments with different angled block arrangements.

0.766, 0.813 and 0.850. The evolution of axial stress–strain curves are depicted in Fig. 15 for different initial relative densities. The numerical results are in very good agreement with the experiments given in this figure, and the only major difference appears in the non-linear behavior at the beginning of the measured stress–strain curves. This non-linear behavior is attributed to the initial seating and setting errors during the experiments, reported by Gu et al. (2001).

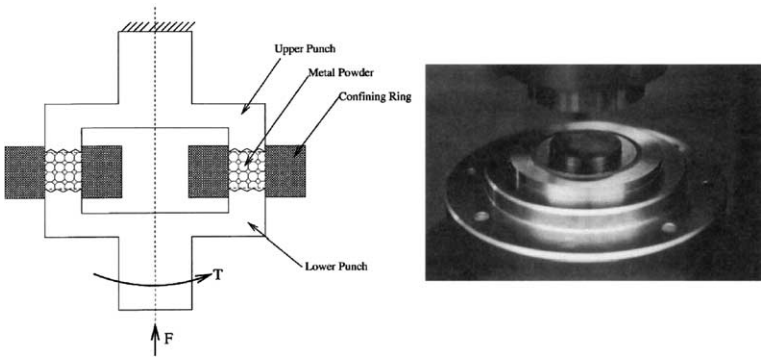

Fig. 12. Schematic of the torsion ring-shear apparatus (Gu et al., 2001).

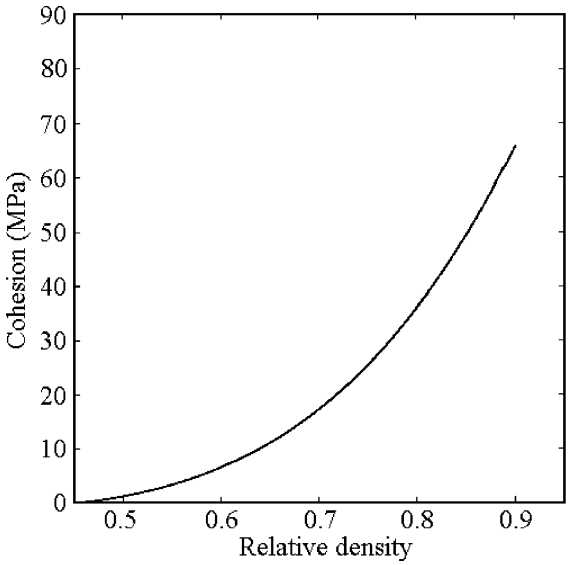

Fig. 13. Variation of the cohesion with relative density for MH-100 iron powder.

5.3.2. Simulation of a compaction process

In order to demonstrate the performance of the present model in simulating the metal powder during compaction process, the uniaxial compaction of a cylindrical MH-100 iron powder component is analysed numerically. The experimental data and numerical results are available for this example and are used for comparison. The powder material is modeled by the endochronic plasticity with the material parameters obtained in previous section and summarized in Box 2. The finite element modeling of the cylindrical component is performed using an axisymmetric representation and a structured mesh of 144 bilinear elements. The initial geometry, boundary conditions and FE mesh are depicted in Fig. 16(a). The die wall friction is simulated with Coulomb friction coefficient $\mu = 0.37$ (Gu et al., 2001) and the initial relative density of the powder is $\eta_0 = 0.42$. The problem has been solved with displacement control by increasing top punch displacement up to 30 mm while the bottom punch is fixed.

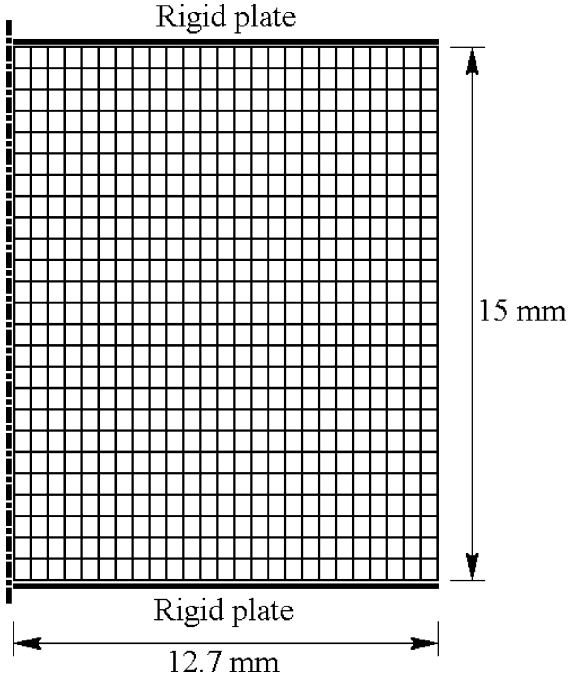

Fig. 14. Simple compression specimen: an axisymmetric FE mesh.

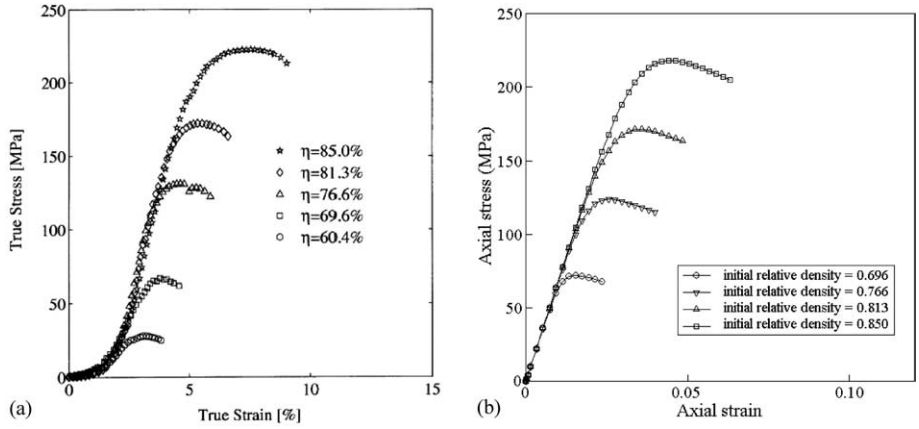

Fig. 15. Simple compression of compacted specimens; axial stress versus axial strain curves for MH-100 iron powder: (a) experimental results (Gu et al., 2001), (b) endochronic model.

The evolution of top punch vertical reaction force with its vertical displacement is depicted in Fig. 16(b). Also plotted in this figure, is the experimental result given by Gu et al. (2001). The result shows a good agreement between the experimental data and numerical simulation obtained by endochronic model. The relative density distribution over the sample at the end of the simulation is depicted in Fig. 17. The relative

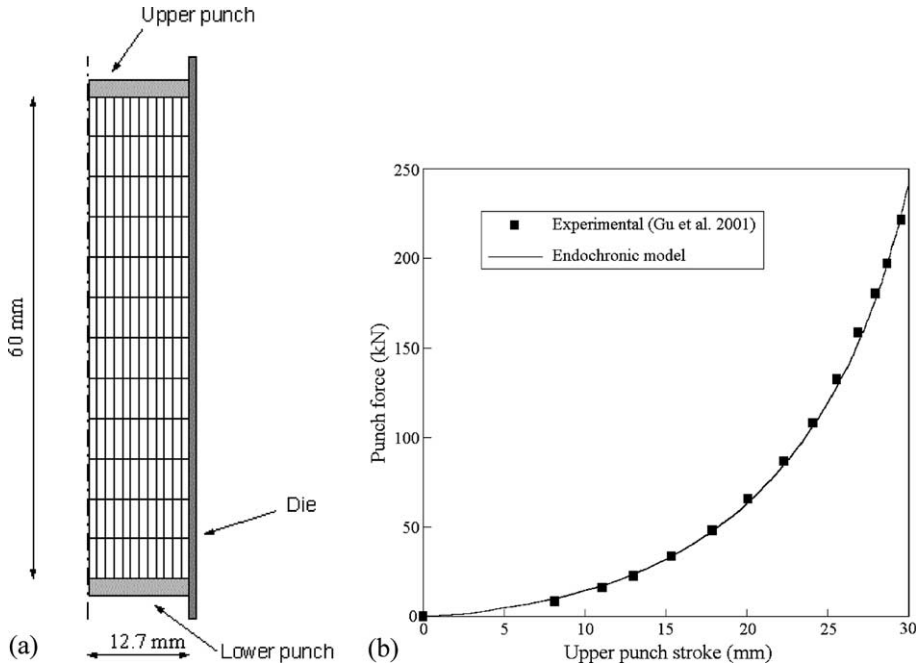

Fig. 16. The uniaxial compaction of cylindrical MH-100 powder component: (a) an axisymmetric FE mesh (after Gu et al., 2001), (b) the variation of top punch vertical reaction with displacement.

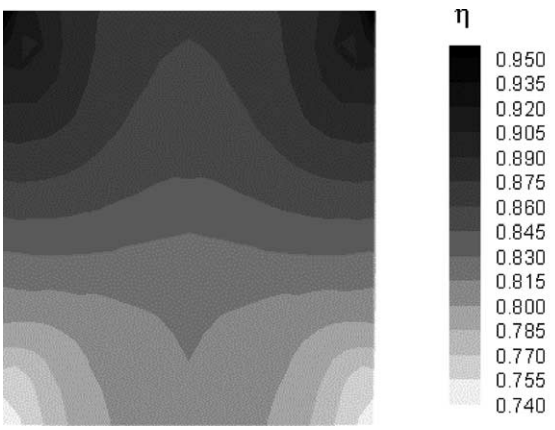

Fig. 17. Cylindrical MH-100 powder component: the calculated density distribution at the final stage of compaction.

density distribution is in complete agreement with those reported by Gu et al. (2001). This example demonstrates that the endochronic model is capable to describe the behavior of MH-100 metal powder in true-triaxial experiments, shear test and axial compression experiments. The results of a powder compaction simulation show how the proposed model can be

Box 2. Endochronic material parameters, MH-100 iron powder

Elastic parameters: $E = 698\exp(5.62\eta)$ MPa, $v = 0.3$
Kernel parameters: $A_1 = 90,000$ MPa, $\alpha_1 = 1000$
$B_1 = 90,000$ MPa, $\beta_1 = 500$, $\beta_2 = 80$, $\beta_3 = 5$
$C_1 = 0, C_2 = 15, C_3 = 1.5$ MPa
Initial relative density: $\eta_0 = 0.45$
Deviatoric scale function parameters:

$$c(\eta) = 1.4\eta^3 \frac{\eta - \eta_0}{1 - \eta_0}, \quad p_0 = 245 \text{ MPa}$$

Hydrostatic scale function parameters:

$$g(\eta) = \eta^{2.5} \frac{\eta - \eta_0}{1 - \eta_0}, \quad \psi = 0.5, \quad \phi_h = 500 \text{ MPa}$$

Coupling parameter: $\kappa = 1.5$

used to predict the density distribution in the compact and punch forces accurately.

6. Conclusions

In the present paper, an advanced theory of plasticity was developed based on an endochronic model for powder forming processes. The cone-cap yield surface was derived from endochronic constitutive equations, assuming a special form for the kernel functions. The flow rule and the dilatancy condition of the proposed plasticity model were derived and a procedure for calibration of material parameters of the model was proposed. A general algorithm for the endochronic theory along with the constitutive equations in finite strain and their numerical integration were established. The elastic response was stated by a hypo-elastic model and endochronic constitutive equations were developed in the unrotated frame of reference. Constitutive equations were obtained based on coupling between deviatoric and hydrostatic behavior through out the endochronic theory for rate-independent, plastically compressible, initially isotropic materials. Finally, the tangent modulus consistent with the integration algorithm of elastic–plastic constitutive equations was extracted.

The material model and numerical schemes were examined for efficacy in the modeling of a multi-level, shaped tablet and cylindrical MH-100 iron powder components. It is demonstrated that the model is capable to describe the behavior of different metal powders in true-triaxial experiments, shear test and axial compression experiments. The results of powder compaction simulations show that the endochronic theory in the context of finite deformation plasticity can be used to predict the density distribution in the compact in an efficient and accurate manner.

Appendix A. Consistent tangent operator

In order to achieve the quadratic convergence rate of Newton method in solving the global system of non-linear equations, it is essential to use the consistent tangent moduli with integration procedure of constitutive equations in forming tangent stiffness matrix (Simo and Taylor, 1985). In this section, the incremental constitutive equations, derived in Section 4, are linearized to yield consistent tangent modulus.

Taking material time derivate of Eqs. (64) and (65) yields

$$\Delta\dot{\hat{\boldsymbol{\sigma}}}_{\rm dev} = \mathbf{H}_1^{\rm dev}\Delta\dot{z}_{\rm d} + H_2^{\rm dev}\Delta\dot{\hat{\mathbf{d}}}_{\rm dev}^{\rm p} \tag{A.1}$$

$$\Delta\dot{\hat{\sigma}}_{\rm h} = H_1^{\rm h}\Delta\dot{z}_{\rm h} + H_2^{\rm h}\Delta\dot{\hat{d}}_{\rm vol}^{\rm p} + H_3^{\rm h}\Delta\dot{\varsigma} + H_4^{\rm h}\boldsymbol{\sigma}_{\rm dev} : \Delta\dot{\hat{\mathbf{d}}}^{\rm p} \tag{A.2}$$

where

$$\mathbf{H}_1^{\rm dev} = 2\frac{\Delta\hat{\mathbf{d}}_{\rm dev}^{\rm p}}{\Delta z_{\rm d}}\sum_{r=1}^{m} A_r {\rm e}^{-\alpha_r\Delta z_{\rm d}} - 2\frac{\Delta\hat{\mathbf{d}}_{\rm dev}^{\rm p}}{\Delta z_{\rm d}^2}\sum_{r=1}^{m}\frac{A_r}{\alpha_r}(1-{\rm e}^{-\alpha_r\Delta z_{\rm d}}) - \sum_{r=1}^{m}\alpha_r{}^n(\hat{\boldsymbol{\sigma}}_{\rm dev}^r){\rm e}^{-\alpha_r\Delta z_{\rm d}} \tag{A.3}$$

$$H_2^{\rm dev} = \frac{2}{\Delta z_{\rm d}}\sum_{r=1}^{m}\frac{A_r}{\alpha_r}(1-{\rm e}^{-\alpha_r\Delta z_{\rm d}}) \tag{A.4}$$

$$H_1^{\rm h} = 2\frac{\Delta\hat{d}_{\rm vol}^{\rm p}}{\Delta z_{\rm h}}\sum_{i=1}^{m} B_i{\rm e}^{-\beta_i\Delta z_{\rm h}} - 2\frac{\Delta\hat{d}_{\rm vol}^{\rm p}}{\Delta z_{\rm h}^2}\sum_{i=1}^{m}\frac{B_i}{\beta_i}(1-{\rm e}^{-\beta_i\Delta z_{\rm h}}) - \sum_{i=1}^{m}\beta_i{}^n\left(\hat{\sigma}_{\rm h}^i\right){\rm e}^{-\beta_i\Delta z_{\rm h}} + \frac{2\boldsymbol{\sigma}_{\rm dev} : \Delta\hat{\mathbf{d}}^{\rm p}}{\Delta\varsigma}\sum_{i=1}^{m} C_i{\rm e}^{-\beta_i\Delta z_{\rm h}} \tag{A.5}$$

$$H_2^{\rm h} = \frac{2}{\Delta z_{\rm h}}\sum_{i=1}^{m}\frac{B_i}{\beta_i}(1-{\rm e}^{-\beta_i\Delta z_{\rm h}}) \tag{A.6}$$

$$H_3^{\rm h} = -\frac{2\boldsymbol{\sigma}_{\rm dev} : \Delta\hat{\mathbf{d}}^{\rm p}}{\Delta\varsigma^2}\sum_{i=1}^{m}\frac{C_i}{\beta_i}(1-{\rm e}^{-\beta_i\Delta z_{\rm h}}) \tag{A.7}$$

$$H_4^{\rm h} = \frac{2}{\Delta\varsigma}\sum_{i=1}^{m}\frac{C_i}{\beta_i}(1-{\rm e}^{-\beta_i\Delta z_{\rm h}}) \tag{A.8}$$

In order to linearize $\Delta z_{\rm d}$ and $\Delta z_{\rm h}$, the relative density η, Lode's angle θ and intrinsic time ς, should be determined. For this purpose, taking the time derivative from Eq. (8) and applying the identity of $\partial J/\partial\mathbf{U} = J\mathbf{U}^{-1}$, we will arrive to

$$\dot{\eta} = -\eta\mathbf{U}^{-1} : \dot{\mathbf{U}} \tag{A.9}$$

Using Eq. (55), $\dot{\mathbf{U}}$ can be stated in terms of $\Delta\hat{\mathbf{d}}$ as

$$\Delta t\dot{\mathbf{U}} = \mathbf{Q}^{-1} : \Delta\hat{\mathbf{d}} \tag{A.10}$$

where the fourth-order tensor $\mathbf{Q}$ is defined as

$$\mathbf{Q}_{ijkl} = \frac{1}{4}\left(\delta_{ik}{}^{n+\frac{1}{2}}\mathbf{U}_{lj}^{-1} + \delta_{il}{}^{n+\frac{1}{2}}\mathbf{U}_{kj}^{-1} + \delta_{jl}{}^{n+\frac{1}{2}}\mathbf{U}_{ik}^{-1} + \delta_{jk}{}^{n+\frac{1}{2}}\mathbf{U}_{il}^{-1}\right) \tag{A.11}$$

Applying relations (6), (41) and (54) and considering $\dot{J}_2 = -\hat{\boldsymbol{\sigma}}_{\rm dev} : \dot{\hat{\boldsymbol{\sigma}}}_{\rm dev}$ and $\dot{J}_3 = J_3\hat{\boldsymbol{\sigma}}_{\rm dev}^{-1} : \dot{\hat{\boldsymbol{\sigma}}}_{\rm dev}$, it yields

$$\dot{\theta}\Delta t = \mathbf{Y} : (\Delta\hat{\mathbf{d}} - \Delta\hat{\mathbf{d}}^{\rm p}) \tag{A.12}$$

where

$$\mathbf{Y}_{ij} = \frac{-2\sqrt{3}\mu J_3}{\sqrt{4J_2^3 - 27J_3^2}}\left(\frac{3}{2J_2}\left(\hat{\boldsymbol{\sigma}}_{ij} - \frac{1}{3}\hat{\boldsymbol{\sigma}}_{kk}\delta_{ij}\right) + \left(\hat{\boldsymbol{\sigma}}_{\rm dev}^{-1}\right)_{ij} - \frac{1}{3}\left(\hat{\boldsymbol{\sigma}}_{\rm dev}^{-1}\right)_{kk}\delta_{ij}\right) \tag{A.13}$$

where $\Delta\dot{\varsigma}$ can be obtained by taking time derivative from Eq. (67) as

$$\Delta\dot{\varsigma} = \frac{1}{\Delta\varsigma}\Delta\hat{\mathbf{d}}^{\mathrm{p}}_{\mathrm{dev}} : \Delta\dot{\hat{\mathbf{d}}}^{\mathrm{p}} + \frac{\kappa^2}{\Delta\varsigma}\Delta\hat{d}^{\mathrm{p}}_{\mathrm{vol}}\Delta\dot{\hat{d}}^{\mathrm{p}}_{\mathrm{vol}} \tag{A.14}$$

Taking material time derivative of Eq. (68) yields

$$\Delta\dot{z}_{\mathrm{d}} = \frac{\Delta\dot{\varsigma}}{f_{\mathrm{d}}} - \frac{\Delta\varsigma}{f_{\mathrm{d}}^2}\left(\frac{\partial f_{\mathrm{d}}}{\partial p}\dot{p} + \frac{\partial f_{\mathrm{d}}}{\partial \eta}\dot{\eta} + \frac{\partial f_{\mathrm{d}}}{\partial \theta}\dot{\theta}\right) \tag{A.15}$$

Applying similar procedure to Eq. (69) yields

$$\Delta\dot{z}_{\mathrm{h}} = \frac{\Delta\dot{\varsigma}}{\kappa f_{\mathrm{h}}} - \frac{\Delta\varsigma}{\kappa f_{\mathrm{h}}^2}\left(\frac{\partial f_{\mathrm{h}}}{\partial p}\dot{p} + \frac{\partial f_{\mathrm{h}}}{\partial \eta}\dot{\eta}\right) \tag{A.16}$$

Substituting Eqs. (A.1), (A.7), (A.12), (A.14), (A.15) and (A.16) in time derivative equation (47), by lengthy but straightforward calculation yields

$$\dot{\hat{\boldsymbol{\sigma}}} = \boldsymbol{N} : \Delta\dot{\hat{\mathbf{d}}}^{\mathrm{p}} + \mathbf{P} : \Delta\dot{\hat{\mathbf{d}}} \tag{A.17}$$

where

$$\boldsymbol{N} = \boldsymbol{N}^a + \boldsymbol{N}^b + \boldsymbol{N}^c \tag{A.18}$$

and

$$\boldsymbol{P} = \boldsymbol{P}^a + \boldsymbol{P}^b + \boldsymbol{P}^c \tag{A.19}$$

where tensors $\boldsymbol{N}^a$, $\boldsymbol{N}^b$, $\boldsymbol{N}^c$, $\boldsymbol{P}^a$, $\boldsymbol{P}^b$, $\boldsymbol{P}^c$ and $\boldsymbol{I}^{\mathrm{dev}}$ are defined as

$$\boldsymbol{N}^a = \left(H_2^{\mathrm{h}} + KH_1^{\mathrm{h}}\frac{\Delta\varsigma}{\kappa f_{\mathrm{h}}^2}\frac{\partial f_{\mathrm{h}}}{\partial p} + \frac{\kappa^2}{\Delta\varsigma}\left(H_3^{\mathrm{h}} + \frac{H_1^{\mathrm{h}}}{\kappa f_{\mathrm{h}}}\right)\Delta\hat{d}^{\mathrm{p}}_{\mathrm{vol}}\right)\mathbf{I}\otimes\mathbf{I} \tag{A.20}$$

$$\boldsymbol{N}^b = H_2^{\mathrm{d}}\boldsymbol{I}^{\mathrm{dev}} + H_4^{\mathrm{h}}\mathbf{I}\otimes\hat{\boldsymbol{\sigma}}_{\mathrm{dev}} + \left(K\frac{\Delta\varsigma}{f_{\mathrm{d}}^2}\frac{\partial f_{\mathrm{d}}}{\partial p} + \frac{\kappa^2}{f_{\mathrm{d}}\Delta\varsigma}\Delta\hat{d}^{\mathrm{p}}_{\mathrm{vol}}\right)\mathbf{H}_1^{\mathrm{d}}\otimes\mathbf{I} \tag{A.21}$$

$$\boldsymbol{N}^c = \frac{\Delta\varsigma}{f_{\mathrm{d}}^2}\frac{\partial f_{\mathrm{d}}}{\partial\theta}\mathbf{H}_1^{\mathrm{d}}\otimes\mathbf{Y} + \frac{1}{\Delta\varsigma f_{\mathrm{d}}}\mathbf{H}_1^{\mathrm{d}}\otimes\Delta\hat{\mathbf{d}}^{\mathrm{p}}_{\mathrm{dev}} + \frac{1}{\Delta\varsigma}\left(H_3^{\mathrm{h}} + \frac{H_1^{\mathrm{h}}}{\kappa f_{\mathrm{h}}}\right)\mathbf{I}\otimes\Delta\hat{\mathbf{d}}^{\mathrm{p}}_{\mathrm{dev}} \tag{A.22}$$

$$\boldsymbol{P}^a = -\frac{\Delta\varsigma}{f_{\mathrm{d}}^2}\frac{\partial f_{\mathrm{d}}}{\partial\theta}\mathbf{H}_1^{\mathrm{d}}\otimes\mathbf{Y} \tag{A.23}$$

$$\boldsymbol{P}^b = H_1^{\mathrm{h}}\eta\frac{\Delta\varsigma}{\kappa f_{\mathrm{h}}^2}\frac{\partial f_{\mathrm{h}}}{\partial\eta}\mathbf{I}\otimes(\mathbf{U}^{-1}:\mathbf{Q}^{-1}) + \eta\frac{\Delta\varsigma}{f_{\mathrm{d}}^2}\frac{\partial f_{\mathrm{d}}}{\partial\eta}\mathbf{H}_1^{\mathrm{d}}\otimes(\mathbf{U}^{-1}:\mathbf{Q}^{-1}) \tag{A.24}$$

$$\boldsymbol{P}^c = -KH_1^{\mathrm{h}}\frac{\Delta\varsigma}{\kappa f_{\mathrm{h}}^2}\frac{\partial f_{\mathrm{h}}}{\partial p}\mathbf{I}\otimes\mathbf{I} - K\frac{\Delta\varsigma}{f_{\mathrm{d}}^2}\frac{\partial f_{\mathrm{d}}}{\partial p}\mathbf{H}_1^{\mathrm{d}}\otimes\mathbf{I} \tag{A.25}$$

$$\boldsymbol{I}^{\mathrm{dev}}_{ijkl} = \frac{1}{2}(\delta_{ik}\delta_{jl} + \delta_{il}\delta_{jk}) - \frac{1}{3}\delta_{ij}\delta_{kl} \tag{A.26}$$

Taking material time derivative from Eq. (66) and substituting the result in Eq. (A.17), gives

$$\dot{\hat{\boldsymbol{\sigma}}} = \overline{\boldsymbol{C}}^{\mathrm{p}} : \Delta\dot{\hat{\mathbf{d}}} \tag{A.27}$$

where

$$\overline{\boldsymbol{C}}^{\mathrm{p}} = \boldsymbol{C}^{\mathrm{e}}(\boldsymbol{C}^{\mathrm{e}} + \boldsymbol{N})^{-1}(\boldsymbol{P} + \boldsymbol{N}) \tag{A.28}$$

In order to complete the derivation of consistent modulus, the linearization of ${}^{n+1}\mathbf{R}$ and $\Delta\hat{\mathbf{d}}$ is necessary. For consistent linearization of ${}^{n+1}\mathbf{R}$, we start by relation

$$\mathbf{L} = \dot{\mathbf{F}}\mathbf{F}^{-1} = \mathbf{R}\mathbf{R}^{\mathrm{T}} + \mathbf{R}\dot{\mathbf{U}}\mathbf{U}^{-1}\mathbf{R}^{\mathrm{T}} \tag{A.29}$$

Pre-multiplying Eq. (A.29) by $\mathbf{R}^{\mathrm{T}}$ and post-multiplying by $\mathbf{F}$ yields

$$\mathbf{R}^{\mathrm{T}}\mathbf{L}\mathbf{F} = \mathbf{R}^{\mathrm{T}}\dot{\mathbf{R}}\mathbf{U} + \dot{\mathbf{U}} \tag{A.30}$$

Subtracting (A.30) from its transpose, after some manipulation results in

$$\dot{\mathbf{R}} = \boldsymbol{G} : \mathbf{L} \tag{A.31}$$

where

$$\boldsymbol{G}_{ijkl} = (\mathbf{R}_{im}\mathbf{U}_{jn} - \mathbf{R}_{in}\mathbf{U}_{jm})^{-1}(\mathbf{R}_{km}\mathbf{F}_{\ln} - \mathbf{R}_{kn}\mathbf{F}_{lm}) \tag{A.32}$$

Substituting Eq. (A.31) to (A.30) gives $\dot{\mathbf{U}}$ in terms of $\mathbf{L}$ as

$$\dot{\mathbf{U}} = \boldsymbol{H} : \mathbf{L} \tag{A.33}$$

where

$$\boldsymbol{H}_{ijkl} = (\mathbf{R}_{ki}\mathbf{F}_{lj} - \mathbf{R}_{mi}\mathbf{U}_{nj}\mathbf{G}_{mnkl}) \tag{A.34}$$

Applying relation (55) to evaluate $\Delta\dot{\hat{\mathbf{d}}}$ appeared in Eq. (A.27), we obtain

$$\dot{\hat{\mathbf{d}}} = \widetilde{\mathbf{G}} : {}^{n+1}\dot{\mathbf{U}} \tag{A.35}$$

where

$$\widetilde{\mathbf{G}}_{ijkl} = \frac{1}{2}\left({}^{n+\frac{1}{2}}\mathbf{U}^{-1}_{kj}\delta_{il} + {}^{n+\frac{1}{2}}\mathbf{U}^{-1}_{ik}\delta_{jl} - \frac{1}{2}\Delta\mathbf{U}_{im}\,{}^{n+\frac{1}{2}}\mathbf{U}^{-1}_{mk}\,{}^{n+\frac{1}{2}}\mathbf{U}^{-1}_{lj} - \frac{1}{2}\Delta\mathbf{U}_{mj}\,{}^{n+\frac{1}{2}}\mathbf{U}^{-1}_{ik}\,{}^{n+\frac{1}{2}}\mathbf{U}^{-1}_{lm}\right) \tag{A.36}$$

Substituting Eq. (A.33) in (A.35) yields,

$$\dot{\hat{\mathbf{d}}} = \widetilde{\boldsymbol{H}} : \mathbf{L} \tag{A.37}$$

where $\widetilde{\boldsymbol{H}}$ is a fourth-order tensor given as

$$\widetilde{\boldsymbol{H}} = \widetilde{\mathbf{G}} : \mathbf{H} \tag{A.38}$$

Substituting Eq. (A.37) into Eq. (A.27) yields

$$\dot{\hat{\boldsymbol{\sigma}}} = \boldsymbol{C} : \mathbf{L} \tag{A.39}$$

where

$$\boldsymbol{C}_{ijkl} = \overline{\boldsymbol{C}}^{\mathrm{p}}_{ijmn}\widetilde{\boldsymbol{H}}_{mnkl} \tag{A.40}$$

Applying Eqs. (A.31) and (A.39) along with $\dot{\hat{\boldsymbol{\sigma}}} = \mathbf{R}^{\mathrm{T}}\dot{\boldsymbol{\sigma}}\mathbf{R} + \dot{\mathbf{R}}^{\mathrm{T}}\boldsymbol{\sigma}\mathbf{R} + \mathbf{R}^{\mathrm{T}}\boldsymbol{\sigma}\dot{\mathbf{R}}$, yields

$$\dot{\boldsymbol{\sigma}} = \widetilde{\boldsymbol{C}} : \mathbf{L} \tag{A.41}$$

where

$$\widetilde{\boldsymbol{C}}_{ijkl} = \mathbf{R}_{im}\boldsymbol{C}_{mnkl}\mathbf{R}_{jn} - \mathbf{R}_{im}\boldsymbol{G}_{nmkl}\boldsymbol{\sigma}_{nj} - \boldsymbol{\sigma}_{im}\boldsymbol{G}_{mnkl}\mathbf{R}_{jn} \tag{A.42}$$

References

Aydin, I., Briscoe, B.J., Sanliturk, K.Y., 1996. The internal form of compacted ceramic components. A comparison of a finite element modeling with experiment. Powder Technol. 89, 239–254.

Brandt, J., Nilsson, L., 1999. A constitutive model for compaction of granular media, with account for deformation induced anisotropy. Mech. Cohes. Frict. Mater. 4, 391–418.

Brekelmans, W.A.M., Janssen, J.D., Van de Ven, A.A.F., de With, G., 1991. An Eulerian approach for die compaction processes. Int. J. Numer. Methods Eng. 31, 509–524.

Brown, S.B., Weber, G.G.A., 1988. A constitutive model for the compaction of metal powders. Modem Develop. Powder Metall. 18, 465–476.

Chenot, J.L., Bay, F., Fourment, L., 1990. Finite element simulation of metal powder forming. Int. J. Numer. Methods Eng. 30, 1649–1674.

Dienes, J.K., 1979. On the analysis of rotation and stress rate in deforming bodies. Acta Mech. 32, 217–232.

Doremus, P., Geindreau, C., Marttin, A., Debove, L., Lecot, R., Dao, M., 1995. High pressure triaxial cell for metal powder. Powder Metall. 38, 284–287.

Eve, R.A., Reddy, B.D., 1994. The variational formulation and solution of problems of finite strain elastoplasticity based on the use of dissipation function. Int. J. Numer. Methods Eng. 37, 1673–1695.

Fish, J., Shek, K., 2000. Finite deformation plasticity based on additive split of the rate of deformation and hyperelasticity. Comput. Methods Appl. Mech. Eng. 140, 75–93.

Fleck, N.A., 1995. On the cold compaction of powders. J. Mech. Phys. Solids 43, 1409–1431.

Fleck, N.A., Kuhn, L.T., McMeeking, R.M., 1992. Yielding of metal powder bounded by isolated contacts. J. Mech. Phys. Solids 40, 1139.

Gu, C., Kim, M., Anand, L., 2001. Constitutive equations for metal powders: application to powder forming processes. Int. J. Plast. 17, 147–209.

Haggblad, H.A., Oldenburg, M., 1994. Modeling and simulation of metal powder die pressing with use of explicit time integration. Model. Simul. Mater. Sci. Eng. 2, 893–911.

Hsu, S.Y., Griffin, O.H., 1992. On stability and efficiency of numerical integration of endochronic constitutive equations. Comput. Struct. 44, 657–665.

Hsu, S.Y., Griffin, O.H., 1996. Algorithmic tangent matrix approach for mixed hardening model of endochronic plasticity. Comput. Methods Appl. Mech. Eng. 133, 1–14.

Hsu, S.Y., Jain, S.K., Griffin, O.H., 1991. Verification of endochronic theory for nonproportional loading paths. ASCE J. Eng. Mech. 117, 110–131.

Hughes, T.J.R., Winget, J., 1980. Finite rotation effects in numerical integration of rate constitutive equations arising in large deformation analysis. Int. J. Numer. Methods Eng. 15, 1862–1867.

Im, S., Atluri, S.N., 1987. A study of two finite strain plasticity models: an internal time theory using Mandel's director concept and a general isotropic/kinematic hardening theory. Int. J. Plast. 3, 163.

Johnson, G.C., Bammann, D.J., 1984. A discussion of stress rates in finite deformation problems. Int. J. Solids Struct. 20, 725–737.

Khoei, A.R., Lewis, R.W., 1998. Finite element simulation for dynamic large elastoplastic deformation in metal powder forming. Finite Elem. Anal. Des. 30, 335–352.

Khoei, A.R., Lewis, R.W., 1999. Adaptive finite element remeshing in a large deformation analysis of metal powder forming. Int. J. Numer. Methods Eng. 45, 801–820.

Khoei, A.R., Bakhshiani, A., Mofid, M., 2003a. Finite strain endochronic plasticity with reference to metal tube under torsion. Eng. Comput. 20, 248–273.

Khoei, A.R., Bakhshiani, A., Mofid, M., 2003b. An implicit algorithm for hypoelasto-plastic and hypoelasto-viscoplastic endochronic theory in finite strain isotropic-kinematic-hardening model. Int. J. Solids Struct. 40, 3393–3423.

Khoei, A.R., Bakhshiani, A., Mofid, M., 2003c. An endochronic plasticity model for finite strain deformation of powder forming processes. Finite Elem. Anal. Des. 40, 187–211.

Lee, E., 1969. Elastic–plastic deformation at finite strains. J. Appl. Mech. 36, 1–6.

Lewis, R.W., Khoei, A.R., 1998. Numerical modeling of large deformation in metal powder forming. Comput. Methods Appl. Mech. Eng. 159, 291–328.

Lewis, R.W., Khoei, A.R., 2001. A plasticity model for metal powder forming processes. Int. J. Plast. 17, 1659–1692.

Lewis, R.W., Jinka, A.G.K., Gethin, D.T., 1993. Computer aided simulation of metal powder die compaction process. Powder Metall. Int. 25, 287–293.

Lin, H.C., Hsieh, B.J., Valentin, R.A., 1981. The application of endochronic plasticity theory in modeling the dynamic inelastic response of structural systems. Nucl. Eng. Des. 66, 213–221.

McMeeking, R.M., Jefferson, G., Haritos, G.K., 2001. Elastic and viscoelastic response of finite particle junctions in granular materials. In: Zavaliangos, Laptev, (Eds.), Recent Development in Computer Modeling of Powder Metallurgy Process. IOS Press.

Oliver, J., Oller, S., Cante, J.C., 1996. A plasticity model for simulation of industrial powder compaction processes. Int. J. Solids Struct. 33, 3161–3178.

Pan, W.F., Lee, T.H., Yeh, W.C., 1996. Endochronic analysis for finite elastoplastic deformation and application to metal tube under torsion and metal rectangular block under biaxial compression. Int. J. Plast. 12, 1287.

Perez-Foguet, A., Rodriguez-Ferran, A., Huerta, A., 2001. Consistent tangent matrices for density-dependent finite plasticity models. Int. J. Numer. Anal. Methods Geomech. 25, 1045–1075.

Ponthot, J.P., 2002. Unified stress update algorithms for the numerical simulation of large deformation elasto-plastic and elasto-viscoplastic processes. Int. J. Plast. 18, 91–126.

Ransing, R.S., Gethin, D.T., Khoei, A.R., Mosbah, P., Lewis, R.W., 2000. Powder compaction modelling via the discrete and finite element method. J. Mater. Des. 21, 263–269.

Rivlin, R.S., 1981. Some comments on the endochronic theory of plasticity. Int. J. Solids Struct. 17, 231–248.

Sandler, I.S., 1978. On the uniqueness and stability of endochronic theories of material behavior. J. Appl. Mech. 45, 263–266.

Simo, J.C., Taylor, R.L., 1985. Consistent tangent operator for rate-independent elastoplasticity. Comput. Methods Appl. Mech. Eng. 48, 101–118.

Valanis, K.C., 1971. A theory of viscoplasticity without yield surface, Part II. Application to mechanical behavior of metals. Arch. Mech. 23, 535–551.

Valanis, K.C., 1980. Fundamental consequences of a new intrinsic time measure: plasticity as a limit of endochronic theory. Arch. Mech. 32, 171–191.

Valanis, K.C., Fan, J., 1984. A numerical algorithm for endochronic plasticity and comparison with experiment. Comput. Struct. 19, 717–724.

Valanis, K.C., Peters, J.F., 1991. An endochronic plasticity theory with shear-volumetric coupling. Int. J. Numer. Anal. Meth. Geomech. 15, 77–102.

Watanbe, O., Atluri, S.N., 1985. A new endochronic approach to computational elastoplasticity: example of a cyclically loaded cracked plate. ASME, J. Appl. Mech. 52, 857–864.

Wu, H.C., Lu, J.K., Pan, W.F., 1995. Endochronic equations for finite plastic deformation and application to metal tube under torsion. Int. J. Plast. 32, 1079–1097.